Politecnico di Torino

Master Thesis
Projet de fin d'étude

Spectroscopic Synthetic Diagnostic for DTT

Bury Yannig

Subba Fabbio

Academic year 2022–2023

List of Figures

List of Tables

1   Divertor Tokamak Test (DTT)

The development of the Demonstration Fusion Power Plant (DEMO) faces many challenges. One of the main one is to develop heat power exhaust systems able to withstand large power load [4] with a maximum heat flux over tens of megawatt per squared meters. In order to try various techniques of power exhaust, the Divertor Tokamak Test (DTT) is planned to be built in Italy (near Rome) [5].

The main objective of DTT is to test different divertor designs, varying the magnetic field configuration (single null, double null, snowflake, X-divertor or super-X) but also to test liquid metal divertor.

This work aims at improving the tomographic systems of DTT by optimizing the placement of the bolometers or the diodes looking at the plasma in the restricted space available in the vacuum chamber and with a limited number of lines of sight. Then this work aims also at providing possible outputs of tomographic inversions in DTT, based on a SOLPS-ITER [6] simulation featuring neon seeding in order to detach the divertor.

For this work, the CHERAB Python package was chosen as the best tool for tomography since it provides tools to simulate the tokamak, create synthetic plasma, determine the emission from a given plasma composition, mimic realistic observations thanks to ray tracing (Raysect package) and gives tools to perform tomography easily.

The next sections aim at giving the reader the keys to understand physical phenomena taking place in tokamaks, the theory of tomography and the functioning of the ray-tracing tools. Then inputs and outputs of the code and the analysis realised will be presented.

2   Coordinate systems in tokamaks

Dealing with tokamaks require an adapted coordinate system [7]. Among different systems, this report will refer at these one :

- The cylindrical system : (r, θ, z);

- The simple toroidal coordinates : (a, ϕ, θ) where $r = R_0 + a \cos \theta$, R_0 is the major radius and corresponds to the torus axis, a is the minor radius, θ the poloidal angle, ϕ the toroidal angle.

These two first coordinates system are illustrated on the figure 1.

Since the section of a tokamak like DTT is not circular, it's more convenient to use a radial coordinate which is related to the flux surfaces in order to replace a.

The poloidal flux is defined as $\psi_p(f) = \int\limits_{S_p} \vec{B} \mathrm{d}\vec{S}$ with S_p is a ring-shaped ribbon stretched between the magnetic axis and the flux surface f.

The toroidal flux is defined as $\psi_t(f) = \int\limits_{S_t} \vec{B} \mathrm{d}\vec{S}$ where S_t is a poloidal section of the flux surface f [1] (see figure 2).

Poloidal and toroidal fluxes can be used as coordinates to replace a. In this case the coordinate is constant along a flux surface (which is a tube, so in a poloidal section, it's a line), these two coordinates are referred as radial coordinates. The radial coordinate $\rho = \sqrt{\psi}$ can also be used. These coordinates can be linearly normalised with 0 at the magnetic axis and 1 at the separatrix (see figure 3).

However toroidal and poloidal flux coordinates system are valid only inside the separatrix. They can be arbitrarily expanded out of it, but it's not the case in this report.
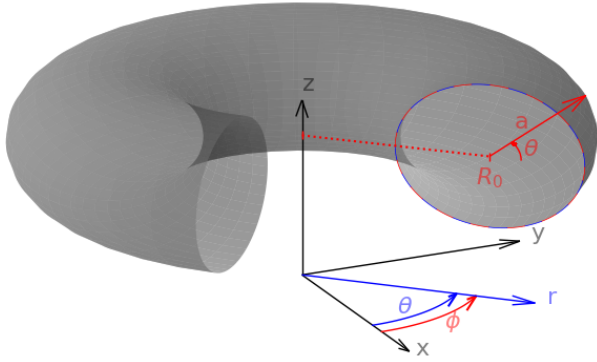
Figure 1: Cylindrical coordinates in blue and simple toroidal coordinates in red.
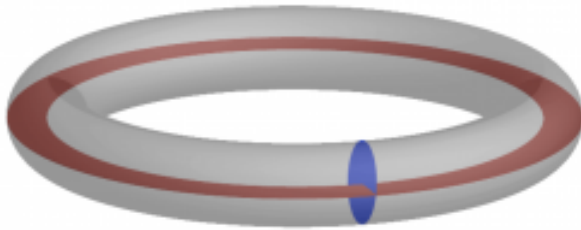
Figure 2: The surfaces used for the definition of poloidal (red) and toroidal flux (blue) [1].
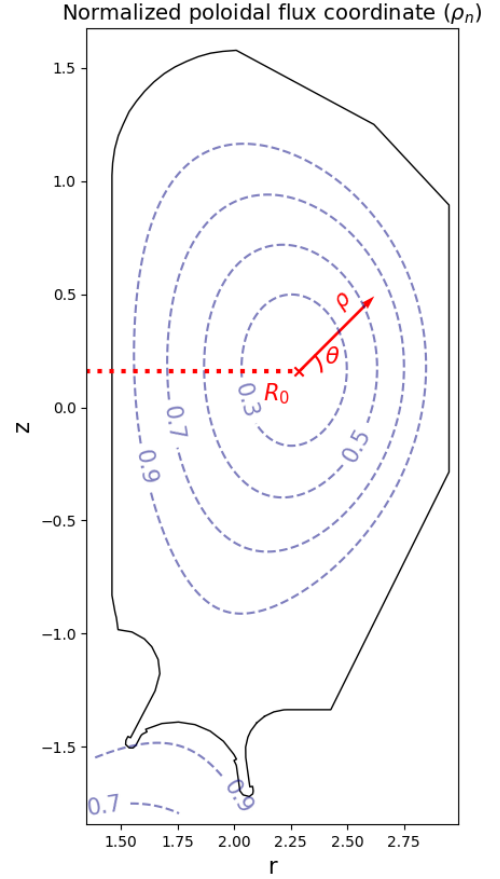
Figure 3: The normalised radial coordinate. Blue lines are isovalues of ρ_n.

3 Light emission

Plasma is a soup of ions and electrons at high temperature moving at high speed. There are different phenomena resulting in light emission or modification, the main ones are line and Bremßtrahlung emission. The two following equations are implemented in CHERAB in the part aiming at computing the emission from a given plasma composition.

3.1 Line radiation

Light is emitted by a simple principle, atoms or ions are excited by a collision with an electron and enters in a metastable state, an electron goes from state i with energy E_i to state k with energy E_k.

For a given species X, excitation is : $X + e^- \longrightarrow X^* + e^-$, then the metastable species returns to a stable state emitting a photon of energy $h\nu = E_j - E_i$: $X^* \longrightarrow X + h\nu$.

After ionisation, recombination processes also emit light : $X + e^- \longrightarrow X^+ + 2e^-$ and $X^+ + e^- \longrightarrow X + h\nu$, resulting in light emission.

Another source of radiation may be charge exchange (CX) between neutrals and ions. It can happens in the case where a neutral beam injector is used, which will not be among the cases studied in this thesis. However, this phenomenon is also common in high-density, low temperature plasma, e. g. near the divertor when a strategy for detached plasma is apply. Since CHERAB only proposes a charge exchange model for beams, it's not possible to introduce this phenomenon in the later analysis.

5

So the light emitted by the transition $E_i \to E_j$ ($\varepsilon_{i \to j}$, in photons·cm^{-3}·s^{-1}) comes from excitation, recombination and charge exchange; this emission is proportional to the density of the species involved and the coefficient of proportionality is the photon emission coefficient (PEC). There are different coefficient depending on the phenomenon involved. Finally the overall emission is [8, 9] :

$$\varepsilon_{i \to j} = \sum_\sigma \text{PEC}_{\sigma, i \to j}^{(exc)} N_e N_\sigma^{z+} + \sum_\rho \text{PEC}_{\rho, i \to j}^{(rec)} N_e N_\rho^{(z+1)+} + \sum_\rho \text{PEC}_{\rho, i \to j}^{(CX)} N_\text{H} N_\sigma^{(z+1)+} \tag{1}$$

With N^{z+} the density of the z-times ionized ion (also called child ion), $N^{(z+1)+}$ the population of the parent ion. ρ and σ correspond to indices of the metastable states of these ions. N_e and N_H are respectively densities of electrons and neutral hydrogen. So $\text{PEC}_{\sigma, i \to j}^{(exc)}$ is the PEC associated to the the metastable state σ and the transition $E_i \to E_j$. The sum over σ means that we include all metastable species capable of the transition $E_i \to E_j$.

3.2 Bremßtrahlung

Bremßtrahlung emission is the emission due to change of direction and acceleration of electrons during elastic collisions with ions. Emissivity of the phenomenon for the wavelength observed λ in Photons·m^{-3}·sr^{-1}·nm^{-1}·s^{-1} is given by [10, 11]:

$$\varepsilon_B (\lambda) = \frac{0.95 \times 10^{-19}}{\lambda \times 4\pi} \times g_{ff} N_e^2 Z_{eff} T_e^{-1/2} \times \exp\left(-\frac{hc}{\sqrt{T_e \times \lambda}}\right) \tag{2}$$

with the electron free-free Gaunt factor $g_{ff} = \max\left(1, 0.6183 \ln\left(T_e\right) - 0.0821\right)$, the electrons temperature T_e in eV, and the wavelength observed λ in nm. h is the Plank constant and c the speed of light both in the international unit system.

4 Tomography

4.1 Introduction

The goal of tomography is to get a view of the section of an object thanks to observations obtained from the exterior of this object. This technique is used in number of fields like medicine, geology, and of course, plasma analysis. In the case of plasma analysis the "object" is the plasma and the goal is to reconstruct the emissivity field in a section of the plasma torus. In all the report below, unless mention of it, tomography will refer to plasma tomography in the frame of a tokamak plasma analysis.

The main difference between plasma tomography and tomography in medicine or geology is the difference in the number of lines of sight which can be big in the case of medicine (of the order of 10^5) while due to the geometric limitations of the tokamak chamber and the changing nature of plasma, very few are available for plasma tomography (from tens to several hundreds).

The plasma tomography aims, e.g., at monitoring the distribution of impurities in the tokamak with a high resolution. This should be done carefully since impurities can limit the steady-state operation or the burning of plasma. These impurities can also be introduced voluntary in order to detach the divertor (i.e. lowering the temperature and the heat flux down to a tolerable level). Tomographic measurements also provide information about the plasma shape.

Tomography is interesting to monitor the plasma because it can overcome the poor accessibility of the hot inner environment (no sensor can be introduced in plasma since it will be destroyed itself and dissipate plasma). Moreover, it can provide a fine resolution, while other instruments just produce a projection view of the plasma (e. g. the view of a regular camera).

Observations for tomography are arrays of line integrated values. Indeed, arrays of sensors are used and each sensor gets the light from plasma after collimation (it can be a narrow pinhole). So these lines where the light is integrated are usually referred to as *lines of sight* (LoS). If there are M sensors, the

observations are arranged into a vector $\vec{f}$ of size M.

A mesh is fitted to the poloidal section analysed. The mesh is composed of N cells. The function $g(\vec{r})$ is the function which gives the emissivity in function of the position coordinate $\vec{r}$. An emissivity profile is described with the vector $\vec{g}$, of size N associated with the mesh.

There are many algorithms to reconstruct the emissivity field. The most commons in the plasma analysis field are presented below.

4.2   Algebraic Reconstruction Technique (ART)

The algebraic reconstruction technique (ART) was presented by Gordon, Bender & Herman in a 1970 paper [12]. Each LoS f_i is defined as follow :

$$f_j = \sum_{i \in \Lambda_j} g_i \tag{3}$$

where Λ_j is the set of cells crossed by the LoS j. The number of elements in Λ_j is N_j (see figure 4).

So, the goal is to reconstruct an emissivity field $\vec{g}_{rec}$ which is as close as possible of $g(\vec{r})$ which is measured with the observations $\vec{f}_{mea}$. A vector $\vec{f}_{rec}$ is defined and should be as close as possible to $\vec{f}_{mea}$.

An initial guess of the emissivity field is produced : $\vec{g}_{rec}^{(0)}$. The following process is made iteratively. At the k-th iteration :

$$f_{rec,j}^{(k)} = \sum_{i \in \Lambda_j} g_{rec,i}^{(k)} \tag{4}$$

Where $\vec{g}_{rec}^{(k)}$ is the k-th approximation of the emissivity field,

- by the *direct multiplicative method*, the emissivity at the cell i is changed according to :

$$\forall i \in \Lambda_j, \quad g_{rec,i}^{(k+1)} = \left(\frac{f_{mea,j}}{f_{rec,j}^{(k)}} \right) g_{rec,i}^{(k)} \tag{5}$$

- by the *direct additive method* :

$$\forall i \in \Lambda_j, \quad g_{rec,i}^{(k+1)} = \max \left(g_{rec,i}^{(k)} + \left(\frac{f_{mea,j} - f_{rec,j}^{(k)}}{N_j} \right) ; 0 \right) \tag{6}$$

Figure 4:   Schematic of the section of a torus (thick black line), the mesh is squared (thin grey lines), the LoS j is shown in red, the cells included in Λ_j are highlighted in blue

Then the process is iterated until $\vec{g}_{rec}$ converged to a certain value. It does not converge at the first iteration because the LoS are crossing, so values in cells of the mesh are overwritten at each iteration.

A factor of 1 of the unit $\dfrac{f_j}{g_i}$ can be used before each g_i in order to ensure consistency of equations (3) and (4).

4.3   Simultaneous Algebraic Reconstruction Technique (SART)

The SART algorithm is an improvement of the ART algorithm presented in 1984 by Andersen & Kak [13]. It uses the sensitivity matrix $\mathbf{T}$ (also called geometric or transition matrix) where each element

T_{ij} is the length of the LoS j in the cell i. It permit to take into account that this length may be very different. So :

$$f_{rec,j} = \sum_{i=1}^{N} T_{ij} g_{rec,i} \tag{7}$$

$$\vec{f}_{rec} = \mathbf{T} \cdot \vec{g}_{rec} \tag{8}$$

Then, iterations are required. From a uniform reconstructed emissivity field at iteration $k = 0$, the following formula is used on every cell $g_{rec,i}$:

$$g_{rec,i}^{(k+1)} = g_{rec,i}^{(k)} + \frac{\sum_j \left(T_{ij} \frac{f_{mea,j} - \vec{T}_j^T \vec{g}_{rec}^{(k)}}{\sum_{i=1}^{N} T_{ij}} \right)}{\sum_j T_{ij}} \tag{9}$$

This algorithm give better reconstructions than the ART algorithm, indeed, there is a reduction in the amplitude of the artifacts. The image is smoother. So it benefits from the fastness of the ART-type algorithms and has the noise suppressive features of the simultaneous reconstruction technique.

A slight improvement can be obtained by replacing the standard correction term:

$$\vec{T}_j \frac{f_{mea,j} - \vec{T}_j^T \vec{g}_{rec}^{(k)}}{\sum_{i=1}^{N} T_{ij}} \tag{10}$$

with a weighted correction term:

$$\vec{w}_j \frac{f_{mea,j} - \vec{T}_j^T \vec{g}_{rec}^{(k)}}{\sum_{i=1}^{N} T_{ij}} \tag{11}$$

where the $\vec{w}_j$ terms are determined thanks to a Hamming window of length N_j (ie all the length of the ray in the reconstruction mesh, see the original article [13]).

4.4 Tikhonov regularisation

This method was presented by Anton *et al.* in 1996 [14]. Similarly than previously, the sensibility matrix is used:

$$\widetilde{\mathbf{T}} \cdot \vec{g}_{rec} = \vec{\widetilde{f}}_{rec} \tag{12}$$

where $\widetilde{T}_{ij} = T_{ij}/\sigma_j$ and $\widetilde{f}_j = f_j/\sigma_j$ with σ_j the standard deviation of the observation f_j.

Since the matrix $\mathbf{T}$ is not squared, it can't be inverted. So the aim is to find $\vec{g}_{rec}$ which minimizes the goodness of fit χ^2:

$$\chi^2 = \left\| \widetilde{\mathbf{T}} \cdot \vec{g}_{rec} - \vec{f}_{mea} \right\|^2 \tag{13}$$

With $\|A\| = A^T \cdot A$ for A a matrix or a vector.

Since there are always fewer equations given by $\vec{f}$ than unknowns ($\vec{g}$), $\chi^2 = 0$ can always be achieved. So there is an infinite number of solutions with $\chi^2 = 0$. The issue is to choose which is the best one of these solutions. So instead of minimizing χ^2 it is better to minimize ϕ:

$$\phi = \frac{1}{2}\chi^2 + \alpha \mathcal{R} \tag{14}$$

with $\mathcal{R}$ a regularisation term. α is the regularisation parameter, a positive number which makes the balance between the regularisation and the goodness of fit. The regularisation term acts as a bias. The solution $\vec{g}$ should not minimize only the goodness of fit parameter, but also minimizes the regularisation term. The regularisation adds many equations (of the order of N), so there are more equations than unknowns and there is only one vector $\vec{g}_{rec}$ which minimizes both the goodness of fit parameter and the regularisation.

Among possible regularisation matrix possible, there are first and second order regularisation. First order regularisation is the minimisation of the gradient. In this case:

$$\mathcal{R} = \|\nabla_x \vec{g}\|^2 + \|\nabla_y \vec{g}\|^2 \tag{15}$$

with $\nabla_x \vec{g}$ and $\nabla_y \vec{g}$ the projections of the gradient $\vec{\nabla} g (\vec{r})$ on the x and y axis.

The solution with the least curvature is the solution selected by the second order regularisation:

$$\mathcal{R} = \|\Delta \vec{g}\|^2 \tag{16}$$

with Δ the Laplacian operator.

In these cases, the best α is determined iteratively, such as $\chi^2 \approx M$, the number of sensors. Indeed, ϕ is a function of α. Each time α is changed, the minimisation of ϕ leads to a different value of χ^2. So it is possible to make vary α in order to obtain χ^2 equals to a certain value (here, the number of sensors).

4.5   Minimisation of the Fisher information

Minimisation of the Fisher Information (MFI) or minimum Fisher regularisation is another regularisation option proposed by Anton in 1996 [14]. The Fisher information is defined as follows:

$$I_F = \int \frac{g'(\vec{r})^2}{g(\vec{r})} \mathrm{d}\vec{r} \tag{17}$$

However, it's not possible to compute directly this function. The process requires to be iterative. The framework is similar tan the previous case, meaning that the algorithm aims at finding the $\vec{g}$ which minimizes 14. In this case, $\mathcal{R}$ becomes $\mathcal{R}^{(n)}$ since the process is iterative.

$$\mathcal{R}^{(n)} = \left\| \sqrt{\mathbf{W}^{(n)}} \cdot \nabla_x \cdot \vec{g}^{(n+1)} \right\|^2 + \left\| \sqrt{\mathbf{W}^{(n)}} \cdot \nabla_y \cdot \vec{g}^{(n+1)} \right\|^2 \tag{18}$$

where $\mathbf{W}^{(n)}$ is diagonal, so $\left(\mathbf{X} = \sqrt{\mathbf{W}^{(n)}} \right) \Leftrightarrow \left(\forall i, X_{ii} = \sqrt{W_{ii}^{(n)}} \right)$ and:

$$W_{ii}^{(n)} = \begin{cases} \frac{1}{g_{rec,i}^{(n)}} & g_{rec,i}^{(n)} > 0 \\ \max(\mathbf{W}) & g_{rec,i}^{(n)} \leq 0 \end{cases} \tag{19}$$

with $\mathbf{W}^{(0)}$ the identity matrix, and finally the iterated emissivity field is found with the minimisation of ϕ:

$$\phi = \frac{1}{2} \left\| \mathbf{T} \cdot \vec{g}_{rec}^{(n+1)} - \vec{f}_{mea} \right\|^2 + \alpha \mathcal{R}^{(n)} \tag{20}$$

The iteration process continues until $\vec{g}_{rec}^{(n)}$ converges.

In the following report, this inversion method is referred to as *Anton's regularisation*.

The algorithm was improved in 2012, presented successively by Mazon, Mlynar and Odstrčil [15, 16, 17]. The improvement is to project the gradient on a base where the axis are parallel and perpendicular to the magnetic flux. This permit to handle the component differently. Indeed, plasma is composed of

ionised particles, so these particles tend to follow the magnetic field line and are distributed differently along and across the same magnetic surface. So these components of the gradient are weighted to give more importance to the parallel component, the effect being that the gradient of the emissivity can be high perpendicularly to the magnetic flux but smooth parallel to the flux.

In this case :

$$\mathcal{R}^{(n)} = \left\| \sqrt{S(\eta) \cdot \mathbf{W}^{(n)}} \cdot \nabla_{//} \cdot \vec{g}^{(n+1)} \right\|^2 + \left\| \sqrt{S(-\eta) \cdot \mathbf{W}^{(n)}} \cdot \nabla_{\perp} \cdot \vec{g}^{(n+1)} \right\|^2 \tag{21}$$

where $\mathbf{W}^{(n)}$ is the same matrix than before and $S(x) = \dfrac{1}{1 + \exp(-x)}$ is the sigmoid function and η is a positive scalar chosen arbitrarily. When $\eta = 0$, the method is equivalent to the Anton one, but when η is too high ($\eta = 5$ for example), the effect of the parallel gradient becomes negligible. Indeed, with $\eta = 5$, contribution of the parallel gradient is less than 1%, with $\eta = 2$, this contribution is 12%. $\eta = 2$ was chosen arbitrarily for all following reconstructions in order to avoid one of the gradient contribution to be negligible.

Then the process is the same than with the Anton's regularisation. This algorithm is referred to as the *Odstrčil's regularisation*.

4.6 Choice of the regularisation parameter for Tikhonov regularisation and MFI

Both Tikhonov regularisation and MFI regularisations require that the user determines the regularisation parameter. The choice of α is made once for the Tikhonov regularisation while it should be determined at each step for the MFI regularisation. The bibliography gives some techniques to determine α.

4.6.1 Division by the standard deviation of the observations

The division of the matrices and vectors by the standard deviation of the observations σ_j as showed in section 4.4. The criterion for α is the $\chi^2 \approx M$. This method cannot be used with numerical standard deviation (coming from a Monte-Carlo process in the ray-tracing for example).

4.6.2 L-curve criterion

The L-curve [18] is the parameterised curve obtained plotting a positive function of the norm of the regularisation $\mathcal{R}$ versus a positive function of the norm of the distance between the reconstructed observations and the experimental ones : $\left\| \mathbf{T}\vec{g}_{rec} - \vec{f} \right\| = \chi$.

The curve created is supposed to have a point of maximum positive curvature, the "corner", giving its L-shape. The value at this corner is a good choice for the regularisation parameter since it is balance between the fitting of the data (χ is low) and the amount of regularisation ($\mathcal{R}$ is low).

As the previous method, this method requires that the inversion must be performed several time in order to find the best α.

4.7 Use of an equation

Another method proposed by Pierre David [19] is to use the following equation :

$$\alpha = \frac{\text{Tr}\left(\mathbf{T}^T\mathbf{T}\right)}{\text{Tr}\left(\mathbf{H}\right)} \tag{22}$$

with $\mathbf{H}$ the regularisation matrix.

- For the 2$^{\text{nd}}$ order regularisation : $\mathbf{H} = \Delta^T\Delta$

- For the Anton's regularisation : $\mathbf{H} = \nabla_x^T \mathbf{W} \nabla_x + \nabla_y^T \mathbf{W} \nabla_y$

- For the Odstrčil's regularisation : $\mathbf{H} = S(\eta) \times \mathbf{B}_{//}^T \mathbf{W} \mathbf{B}_{//} + S(-\eta) \times \mathbf{B}_\perp^T \mathbf{W} \mathbf{B}_\perp$

where the operator $\mathbf{B}$ is the gradient projected on the basis parallel or perpendicular to the magnetic field.

5 CHERAB

CHERAB [11, 20, 2, 21] is a Python library develop by Matthew Carr and Alex Meakins (and other contributors) aiming at modelling plasma diagnostics based on spectroscopic analysis. The functioning is based on Raysect, a ray-tracing engine for geometrical optics applications [22]

5.1 Ray-tracing

The ray-tracing method is based on the simulations of multiple rays from or to a light source in order to reconstruct an image through an observer (an observer can be a camera or any other kind of system which captures light).

The framework is a scene which is composed of 3D modelled solid objects and media absorbing, diffusing, reflecting or refracting light. The ray can either be emitted by a light source, following the paths of light rays, being transformed, going through media modifying the characteristics of the ray (direction, intensity) and often absorbed until reaching the observer. It's forward ray-tracing. However the equations of geometrical optics are reversible, so it's also possible to create rays going from the observer, to a light source, following the reverse path. This is reverse ray-tracing. This reverse method is better from a point of view of computing efficiency, indeed, while with forward modelling computed rays represents all the light rays in the scene, even those which are not important for our application (since they don't reach the observer), reverse modelling has the advantage to model only rays linking the observer and light sources.

Ray-tracing engine are also recursive. When a first ray hit a surface, if the surface is diffusive or reflective (even partly), the hit point is modelled as a source of rays in order to determine what is the light intensity of this surface in order to add its contribution to the first ray.

Finally, once the ray is traced, the path is analysed in order to take into the effects of the media (a gas can absorb light, a plasma may emit light...) on the contribution of the ray.

So, in order to simulate an observer, multiple rays go in random directions from the observer. Then their simulated intensity is averaged in order to obtain the radiant flux absorbed by the sensor.

5.2 Functioning of CHERAB

CHERAB provides many useful tools for the simulation of plasma, including tokamak plasma, for both plasma creation and analysis.

First, plasma can be built by its composition and its temperature. This permit to post-process results of simulations with modelling tools such as SOLPS-ITER. CHERAB, then, is able to compute light emission from this plasma with data from OPEN-ADAS including e.g. PEC relative emissions, Bremßtrahlung phenomena, Doppler phenomena.

With CHERAB, it is also possible to model objects in 3 dimension. These objects can be the environment around the plasma and which interact with lights (reflections, absorption) thanks to the ray-tracing engine. Some tokamak models are provided in sub-packages.

Multiple synthetic sensors are also provided including cameras and bolometers. These sensors can be totally customised (size, shape, frequency range through Raysect).

Finally, tools necessary for tomographic inversion are provided.

5.3 Improvements over other models

The use of Raysect in CHERAB permit to model complex geometries [2]. Indeed, the use of 3D models permit to model occlusion and vignetting (a ray being obstructed by an object, being obstructed by the camera aperture), the calculation of the étendue of a detector (capacity of a detector to accept light) is then closer to the reality and allow to get rid of approximations. So a more realistic model is possible from the geometric point of view.

In the tomography theory, lines of sight are usually modelled as straight thin lines. This approximation is good if the solid angle of a detector is thin. This approximation of the cone by a line can lead to the occlusion of cells especially near a corner. However CHERAB, which uses cones instead of lines permit to avoid these kind of occlusion (see figure 5). Moreover, the transition matrix $\mathbf{T}$ is smoother, giving results closer to the reality.
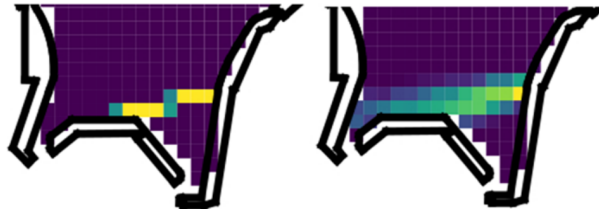

Figure 5: These are representations of the total sensitivity. Cells which are not dark blue are directly influenced by the measurement of the LoS. On the left, a standard modelisation of the LoS by a line, on the right the volume ray-tracing of CHERAB is used (From [2])

6 Framework built for this work

To execute the scripts written for this work, a personal computer was used with the Windows subsystem for Linux (Processor : Intel Core i7-8550U (1.80 GHz) and 16 GB of RAM). So it was not possible to monitor the CPU and RAM resources used.
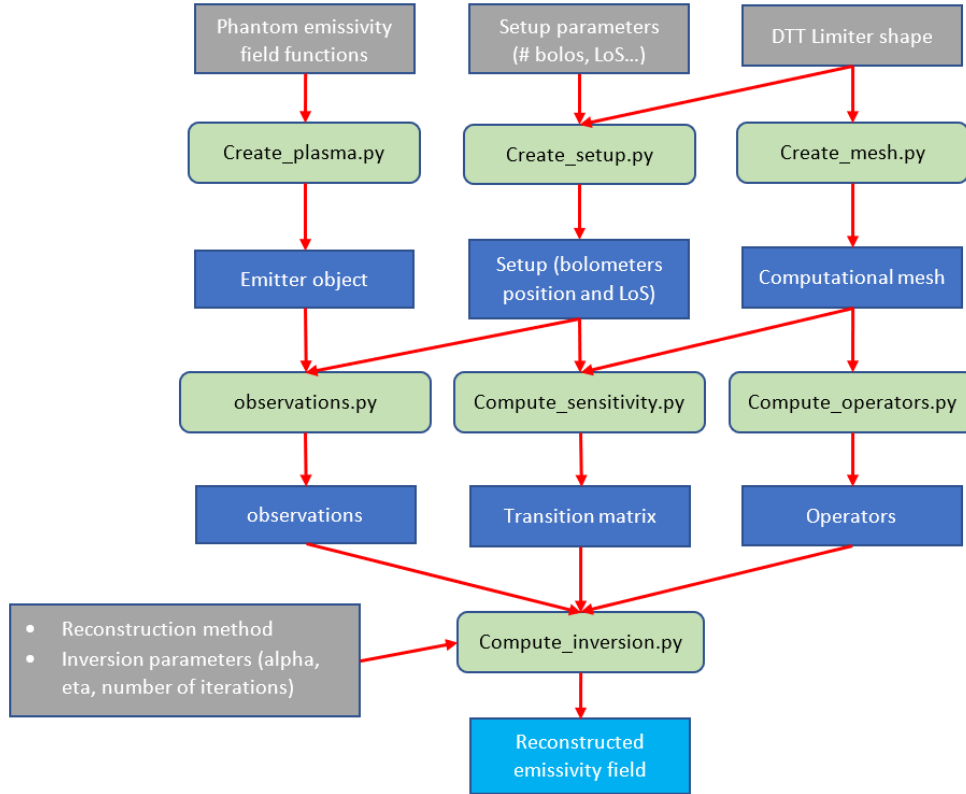

Figure 6: A schematic representing the functioning of the code used for inversions

Figure 6 represents schematically the dependencies between the different files of the script and the "objects" created by each code. Green boxes are main files of the script (there can be some variations in order to perform specific tests, but the logic of the process is still the same), blue boxes are the results provided by each file, grey boxes represents the different parameter inputs in the script. Finally, red arrows represents input and output of each file.

Once the shape of the limiter is input in the code, it is possible to build the mesh which will be the basis of space for the tomographic inversion.

An example of a mesh is presented figure 7. The red line represents the limiter, and all cells are rectangular, almost square (in black). Values which will be computed from this mesh are an average of the field in the cell area. All the plasma chamber is covered, indeed, a cell of the mesh is kept if a section of its area is inside the limiter.

To define the operator matrices only the mesh is required.

With the shape of the limiter and the choices done for a setup (number of bolometers, orientations, positions, angles, number of LoS), it is possible to code the file which will build the setup chosen.

Figure 8 shows an example of setup. The thin grey line is the limiter, the thick black lines show the limits of the vacuum chamber. The aim of the representation of the vacuum chamber is to show the ports where the bolometers will be installed, it has no influence on the observations or the reconstruction process. It permits to materialize the limit of position for the bolometers : not closer than the exterior

wall of the vacuum chamber. Each colored line represents a LoS. The colors have no other meaning than showing the provenance of the LoS and distinguishing them. Large points at the junction of LoS represents the slit of the bolometers. The crosses at their root represent the foils.
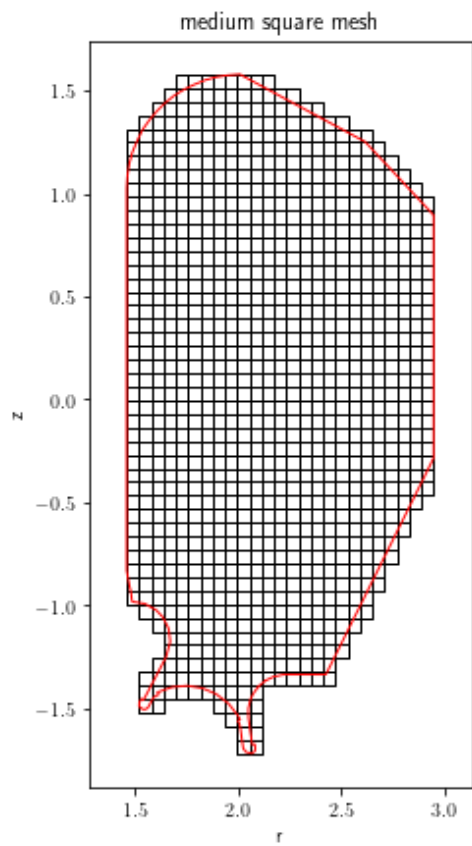

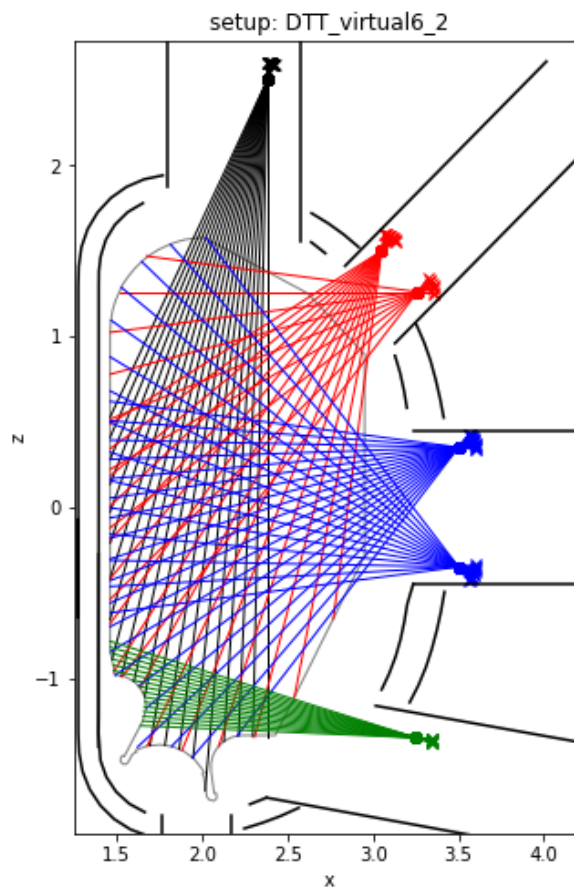Figure 7: Example of a mesh for the tomographic inversion
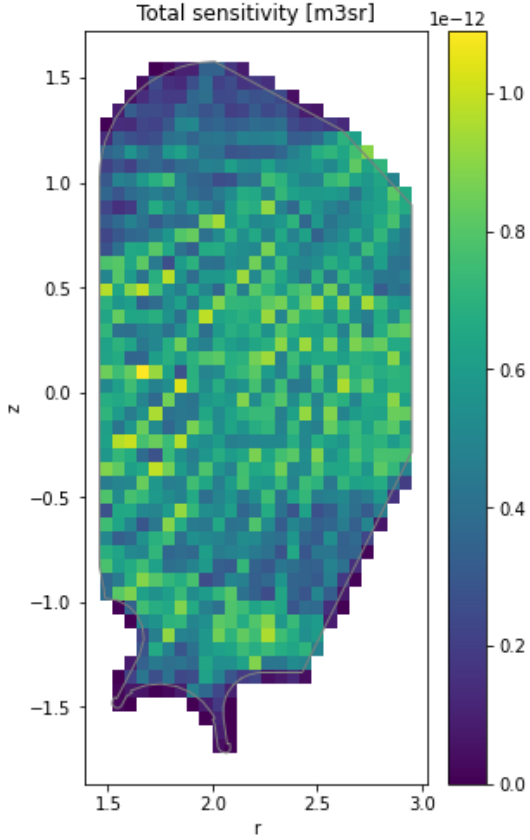

Figure 8: Example of a setup

Figure 9: Total sensitivity of the transition matrix for the previous mesh and setups
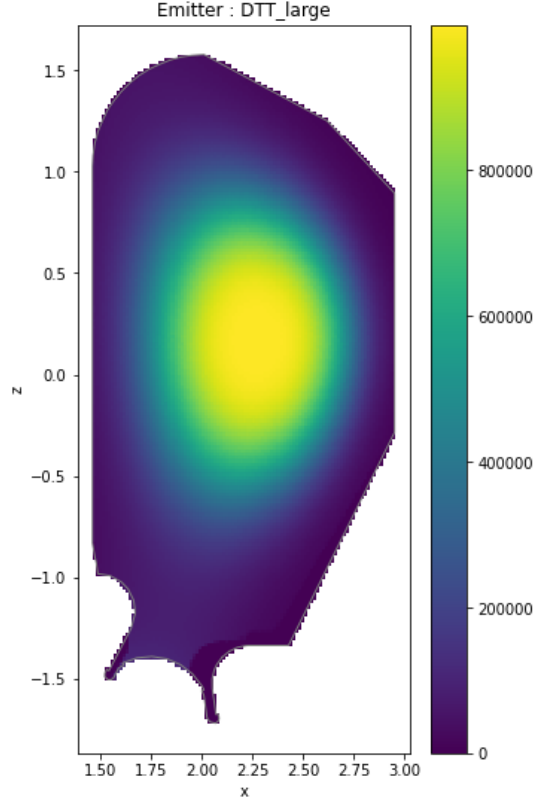
Figure 10: Example of emitter

With the setup and the mesh, it is possible to build the transition matrix.

The example figure 9 shows the total sensitivity (in $m^3 \cdot sr$) for the previous setup. Total sensitivity for the cell i is defined as $\sum_{j=1}^{N} T_{ij}$ with $\mathbf{T}$ the transition matrix. It represents how a cell i is influenced by the output of the bolometers.

The emitter can be defined with arbitrary 2D functions (this is what was done for the analysis of the setups), alternatively it's also possible to define a plasma with its composition (particle type, density, temperature, speed) and with the PEC compute the light emitted by this synthetic plasma.

The example figure 10 shows the emitter "DTT_large" with the light emitted in $W \cdot m^{-3}$. A mesh is used in order to plot this figure, but is not required to create the emitter. Indeed, this emitter is arbitrarily defined as a Gaussian with the radial coordinate ψ and is toroidally symmetric.

With the emitter and the positions of the LoS, the observation vector can be computed thanks to the ray-tracing engine. It represents the output of the sensors for a given emitter.

The figure 11 shows a visual translation of the observation vector $\vec{f}$ for the previous emitter and setup. The thickness of the LoS is proportional to the power received by each sensor. The LoS overlap a representation of the emitter. This plot permit to quickly see which sensors capture the most light (red pointing toward the light emission) and which capture almost nothing in comparison (green).
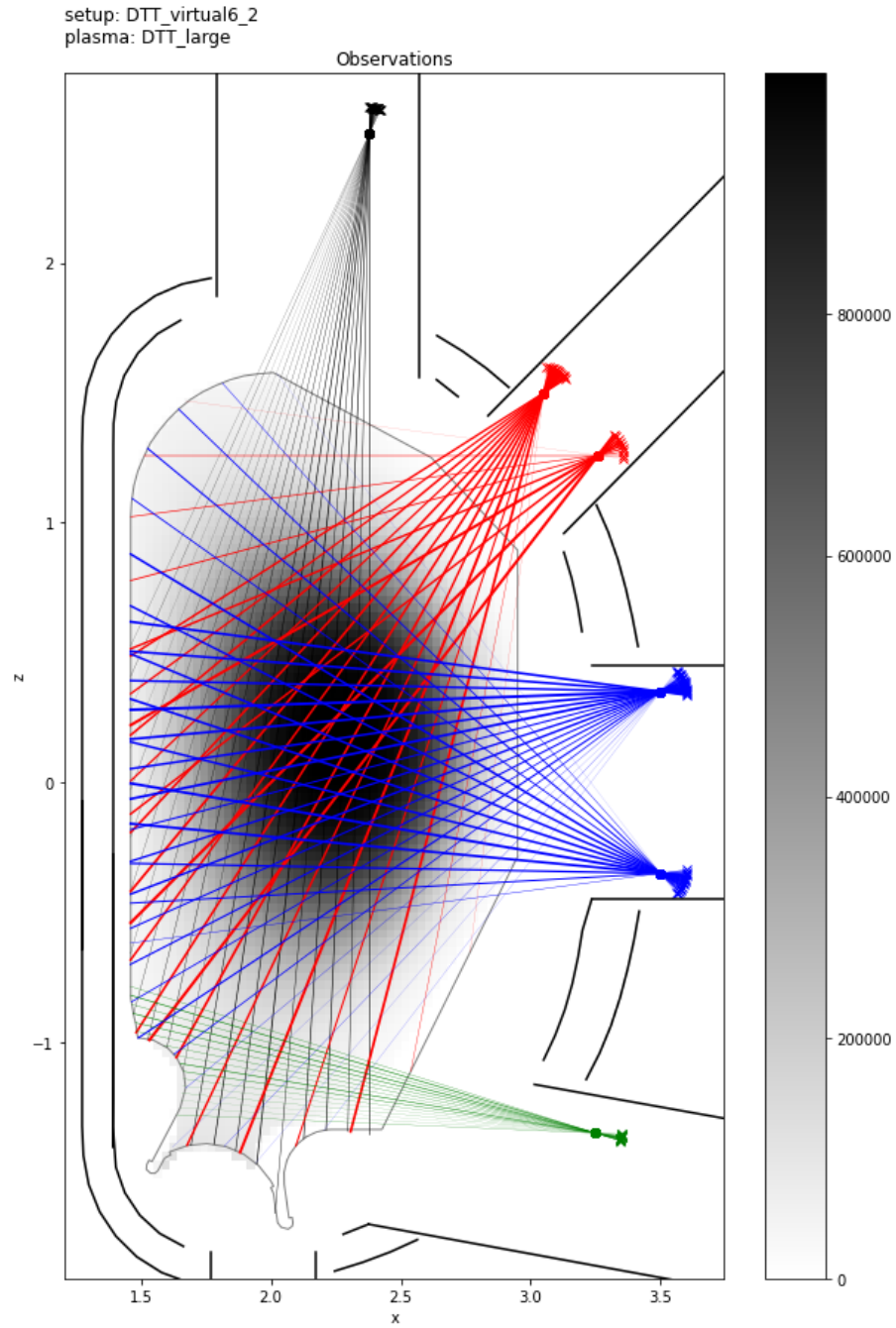
Figure 11: The observation plot, the thickness of each LoS is correlated to the power measured by their respective sensors

Finally, all these matrices (observation vector, transition matrix and operators matrices) are combined with the unknown emissivity field $\vec{g}_{rec}$ in order to perform the reconstruction.

Figure 12 shows the reconstruction for the given observations, mesh, and operators. The left picture shows the phantom, this is what the real emitter looks like. The right one shows the reconstruction. This reconstruction is performed with second order regularisation at an arbitrary regularisation parameter α whose value is showed in the title. α has no unit.

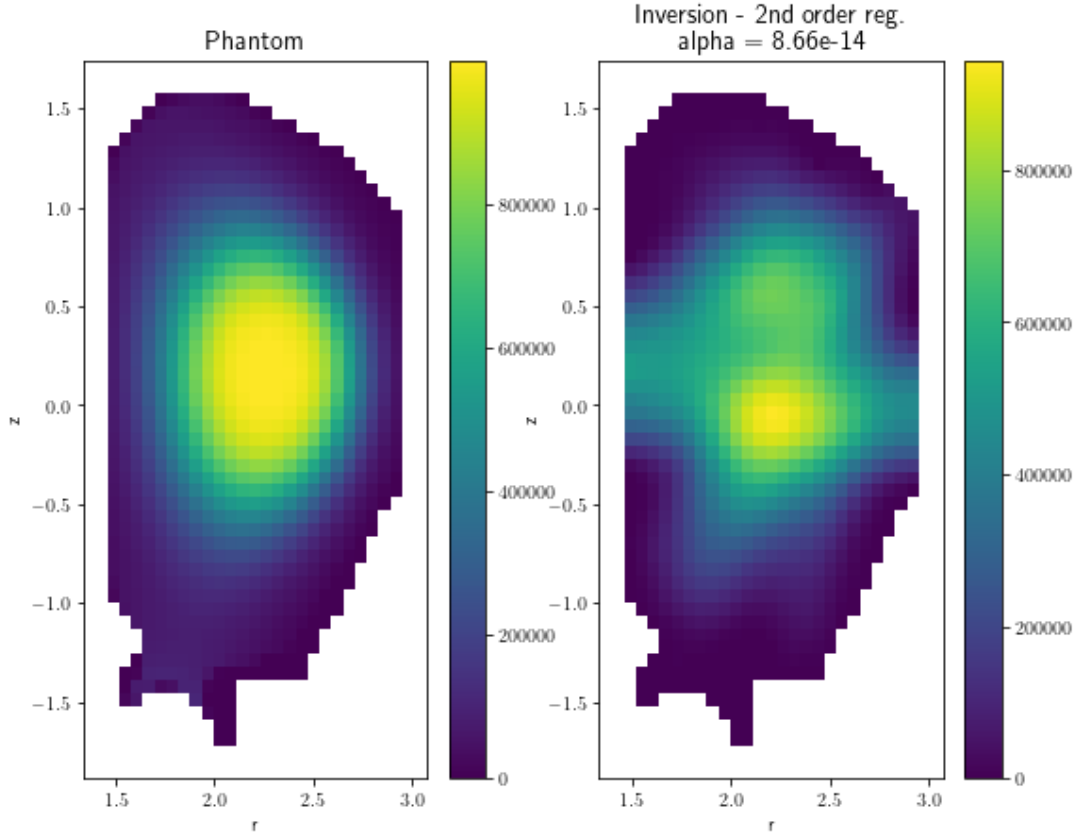Figure 12: The resulting tomographic inversion for the previous mesh, setup and emitter

7 The model of DTT and bolometers in CHERAB

A 3D model was introduced in CHERAB from a given profile (the given profile is the one of the limiter which is clearly visible in figure 11 : it's the thin grey line). For the work, toroidal symmetry of the tokamak limiter is assumed, the consequence is that only a poloidal section of the limiter is necessary to model it. However the simulation is not a 2D simulation but a 3D one (simulations in CHERAB must be realised in a 3D space). The material of the DTT model is tungsten with 10% roughness, indeed DTT is planned to be built in tungsten, the roughness chosen (which impacts reflections, absorption and diffusion) is arbitrarily chosen.

From the CHERAB code [11] : The roughen modifier (the function by which the roughness argument is passed) works by randomly deflecting the surface normal of the geometric model. The deflection is calculated by interpolating between the existing normal and a vector sampled from a cosine weighted hemisphere. The strength of the interpolation, and hence the roughness of the surface, is controlled by the roughness argument, here 10%.
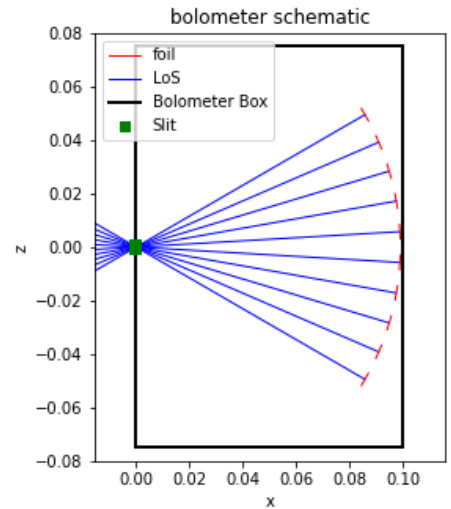

Figure 13: Schematic view of a bolometer. This is a slice view in the plan xz, in the middle of the bolometer. The size of the foils is exaggerated for visibility purposes.

The bolometers are modelled as parallelepipeds (see figure 13), including a small slit (in green in the schematic). The surface of the box of the bolometers is set as a totally absorbing surface as suggested in the examples of the CHERAB code. Rectangular foils (in red) are dispatched in arc around the slit. The distance between the foils and the slit and the height of the foils are set such as all the foils can enter in the box without overlapping whatever is the angle between the LoS and the number of LoS. However the bolometer and foils dimensions should be set in order to obtain a cone of sight with a given angle, but due to the reason presented in the next paragraph, it was not necessary in this work.

The symmetry of the tokamak must be broken in order to create the ports required by the bolometers. Wide cone of sight will be possible. However, in order to reduce the computation time, only holes around the LoS are drilled in the limiter to permit the LoS to "enter" in the chamber. The result of this method (in addition being easy to implement) is that it reduces the computation time of the transition matrix since cones of sights are limited by the hole which acts as a second slit. That's why dimensions of the bolometers weren't based on the opening of the cone of sight.

8   1st and 2nd order operators

The tomography theory requires operators, respectively the gradient for the MFI method and the Laplacian for the second order regularisation. These operators need to be defined as matrices in order to be used on a mesh.

8.1   Gradient
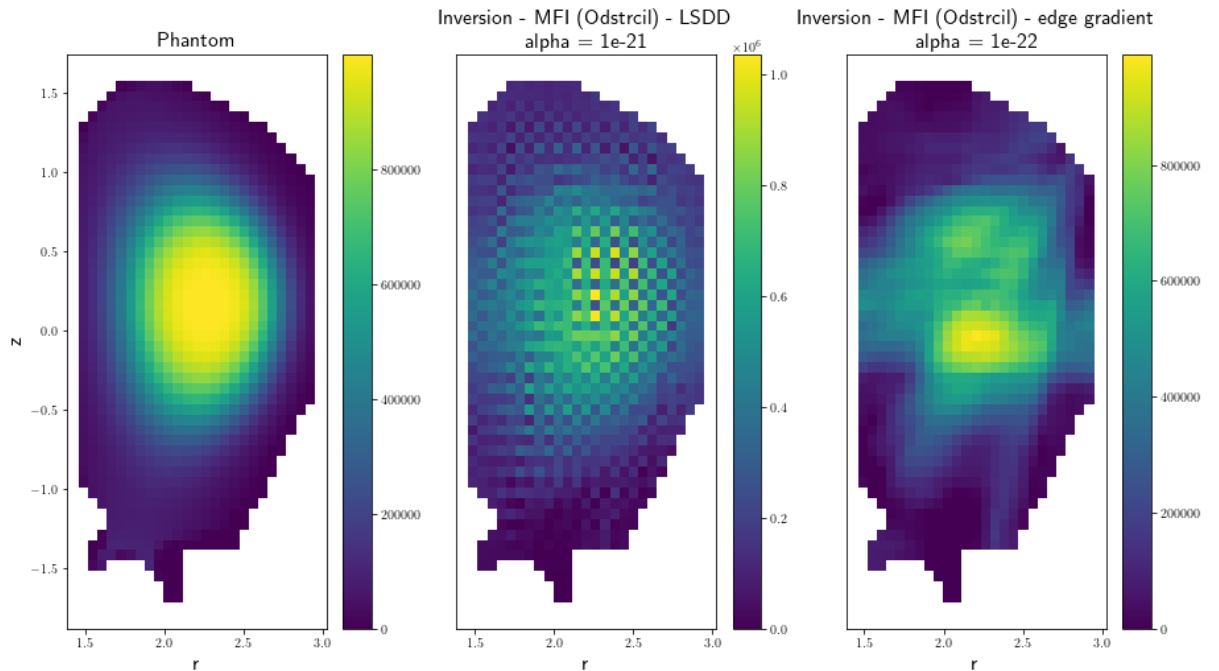
Figure 14: The comparison between the reconstructions with the LSDD gradient (center), the edge gradient (right) and the wished result (left).

The first choice for the gradient equation/matrix was the least square fit of directional derivatives (LSDD) [23] since the equation is applicable on both triangle and square meshes and it takes into account all the surrounding cells and gives pretty accurate results even if it is not really difficult to implement.

However the reconstruction give a pretty strange result, a checkerboard like emissivity field. This result is obviously unphysical and unrealistic. In order to understand this, a return to the theory is necessary. The minimisation of equation 20 means in the MFI case, the minimisation of the gradient, ie, the gradient matrix multiplied by the reconstructed emissivity field. So, the gradient matrix is used to determine what will be the emissivity field, and not just determine the gradient of a given emissivity field, what is usually the case of use of these matrices. As precised earlier, in order to compute the gradient in a first cell, the LSDD method requires the contribution of all surrounding cells, contribution which can be either positive or negative. In the MFI method, the contribution of surrounding cells is also a variable that can be adjusted in order to minimise the gradient (since all cell contributions are part of $\vec{g}_{rec}$). Since the algorithm is free to modify these contributions, the best configuration is chosen for the gradient, which is a succession of high and low contribution, giving this checkerboard like reconstructed emissivity field.

In order to solve this issue, another gradient equation must be chosen. This equation must take into account less parameters in order to reduce the number of degrees of freedom for the MFI method. After multiple tests, in order to avoid this checkerboard like emissivity field, the gradient equation must take into account only two parameters (basic gradient approximation on an axis). So the gradient cannot be expressed in each cell, since it requires to choose two cells among the eight surrounding ones. The gradient must be expressed on the center of each edge of the mesh. Of course the resulting gradient vector has more elements than there are cells, the computation time is then longer. The resulting gradient is also 1 dimensional, it can no longer be expressed in a $r - z$ plane, it is expressed only on the r axis or the z axis.

8.2 Laplacian

The second order regularisation requires a Laplacian as a regularisation matrix. The solution used to determine the Laplacian smoothness operator is the one presented by Carr *et al* [2]. This solution creates the matrix $\mathbf{L}$. For the cell i, the operator value L_{ii} corresponds to the number of neighbours around the cell i, if the cell i is surrounded by cells j, $L_{ij} = -1$, else, $L_{ij} = 0$.

Moreover, in the documentation of CHERAB [11], it is suggested to add a "penalty" to the mesh cells whose total sensitivity is low. Total sensitivity for the cell i is defined as $\sum_{j=1}^{N} T_{ij}$ with $\mathbf{T}$ the transition matrix. If the total sensitivity is among the $x^{th}\%$ lowest, all cells $L_{ij} = 10^5, j \in [1, N]$. Here the *penalty* is 10^5, but it just have to be a really high value. During the reconstruction, the algorithm will avoid to place high emissivity values in the cells where the penalty is applied. The *penalty threshold x* is suggested to be 5% in the documentation of CHERAB.

Empirically, the equation 22 to obtain an adaptive α needs to be modified for $\mathbf{L}$, indeed this equation seems to produce good results :

$$\alpha = \text{Tr}\left(\mathbf{T}^T \mathbf{T}\right) \times \text{Tr}\left(\mathbf{L}\right) \tag{23}$$

9 Reconstruction mesh

The reconstruction algorithms require basis functions on space, which basically means that they require a division of space, a mesh. In order to compare meshes, a statistic is defined, the distance from the phantom. The phantom is the input emitter which is observed and which the reconstruction algorithm aims at reproducing. The distance from the phantom is defined as follow :

$$d = \frac{\|\vec{g}_{rec} - \vec{g}_{ph}\|}{n_{cells}} \tag{24}$$

where $\vec{g}$ is a reconstructed emissivity field decomposed on a mesh : each value of the vector is proportional to the intensity of light in a given cell. The vector is of length N. So $\vec{g}_{ph}$ and $\vec{g}_{rec}$ are respectively the

phantom emissivity field and the reconstructed one. $\|\vec{x}\|$ is the euclidean norm of $\vec{x}$.

The distance from the phantom is a function of α, the regularisation parameter. In the following sections, the "best" reconstruction is the reconstruction which minimizes the distance from the phantom (it is something questionable but this criterion has the benefit to be easy to measure).

9.1 Shape of the mesh

The mesh can either be square or triangular. The square mesh has the benefit to be easy to handle and to implement, however, this mesh is poorly adaptable to curved surfaces as in the divertor area. The triangular mesh solves this problem. However this mesh is harder to handle and control with the tools available on Python, especially the regularity of the size of the cells. Moreover, the examples of tomography in the bibliography show that a square mesh is common. So, all the meshes chosen for tomography are square.

9.2 Size of the mesh

The size of the cells of the mesh is another parameter which can be modified. Basically, a finer mesh permit to obtain more precision and details in the emissivity field and is more adjustable to the geometry of the model. However a finer mesh implies more cells, so more unknowns in the equations for a fixed number of parameters (the number of LoS observing the plasma doesn't change). That's why it is interesting to verify the assumption that a fine mesh is needed.

This verification was carried on with the second order regularisation method. This experiment also permit to verify the threshold of the penalty applied (see 8.2).

In the following pictures, for a unique phantom and a unique setup (setup virtual6_2, providing the best results), different meshes were tested (from mesh 1, the coarsest, to mesh 5, the finest; figures 15 to 19), varying also the penalty threshold from 0% (no penalty) to 15%. The left picture is the phantom emissivity field, the central picture is the best reconstructed emissivity field with the value of the regularisation parameter in the title, and the right graphics show the distance from the phantom in function of alpha, varying the penalty threshold (point color). The penalty threshold whose point is red is the penalty threshold for which the reconstruction is the best. The minimum distance is in the title.
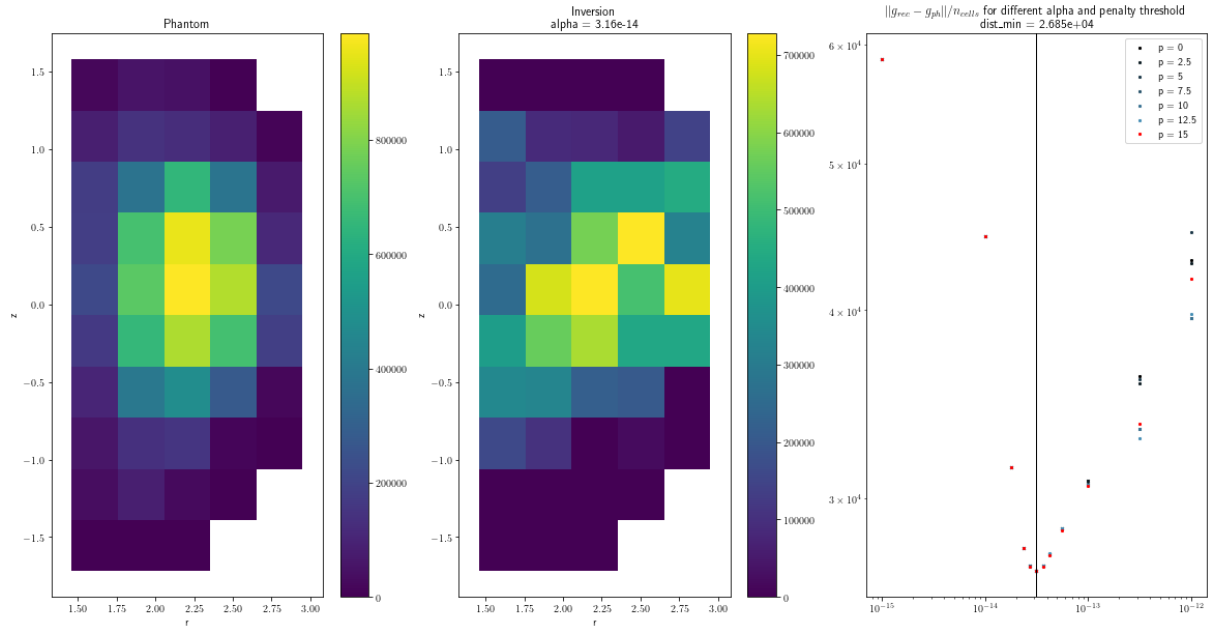
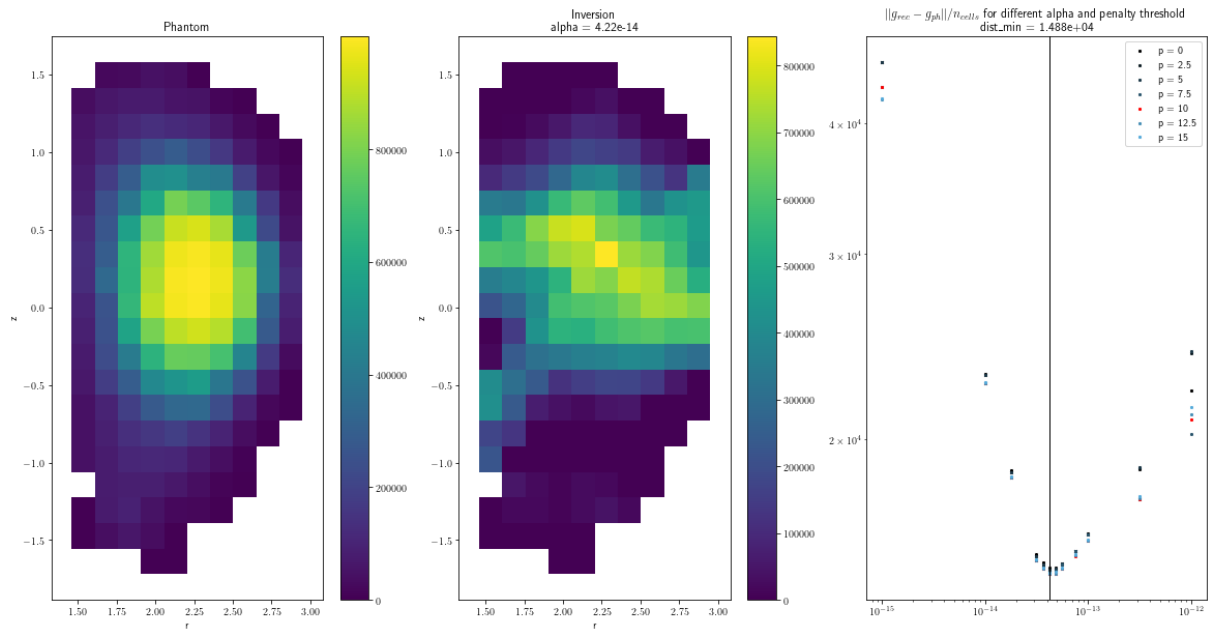Figure 15: Reconstruction with the coarser mesh (mesh 1)

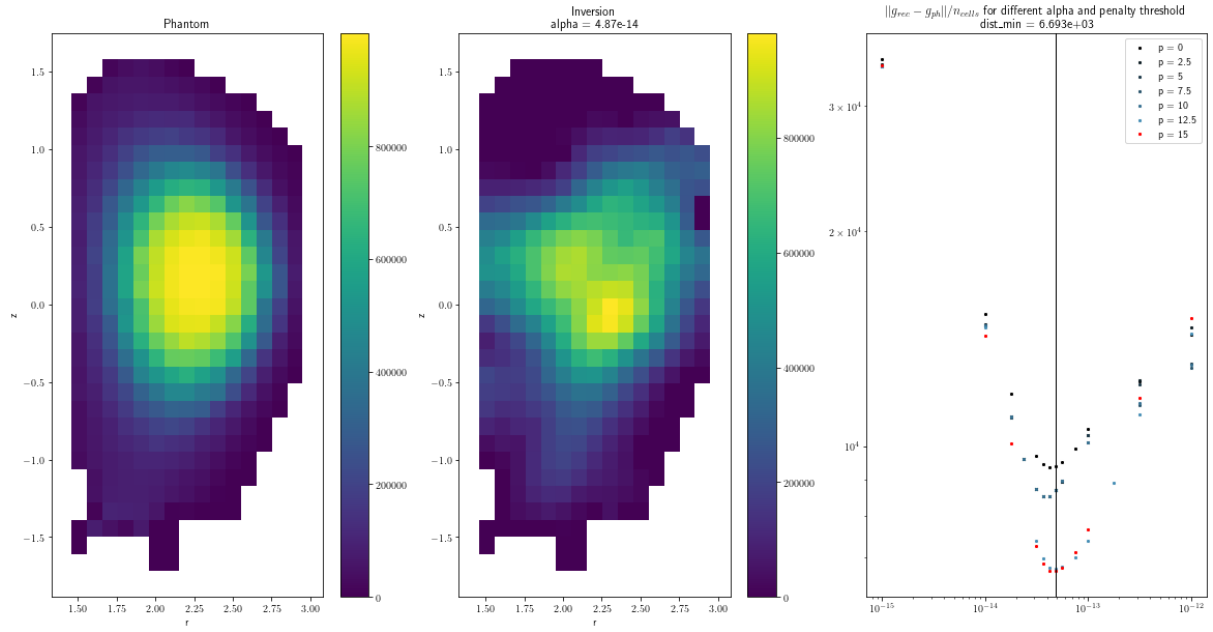Figure 16: Reconstruction with a finer mesh (mesh 2)

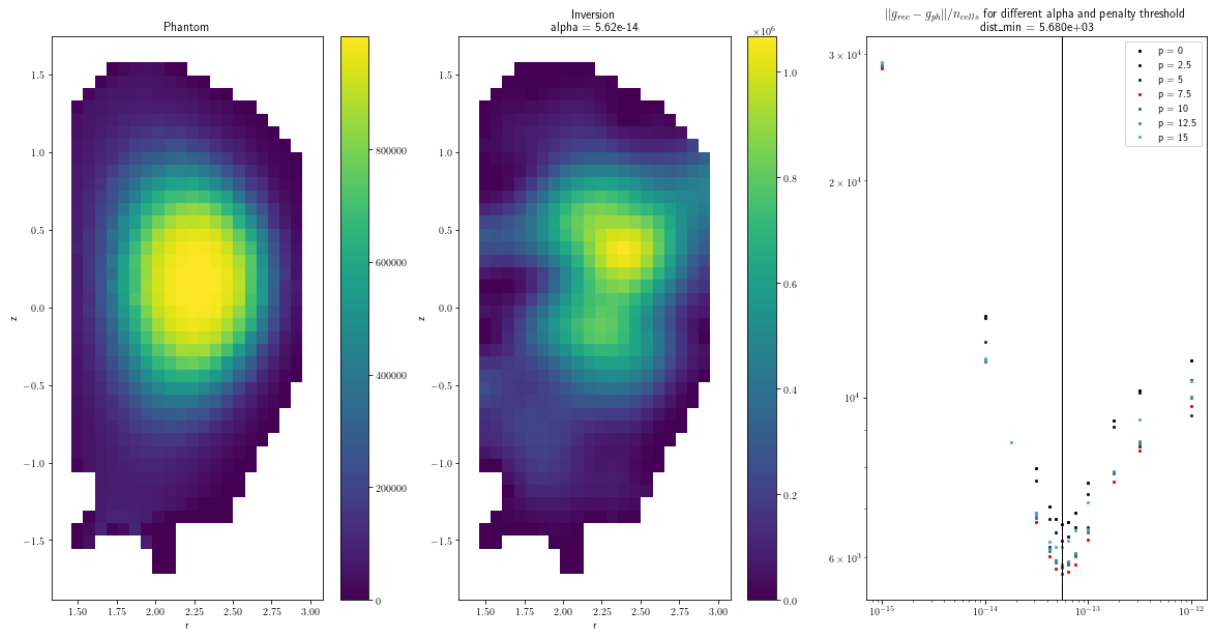Figure 17: Reconstruction with a finer mesh (mesh 3)

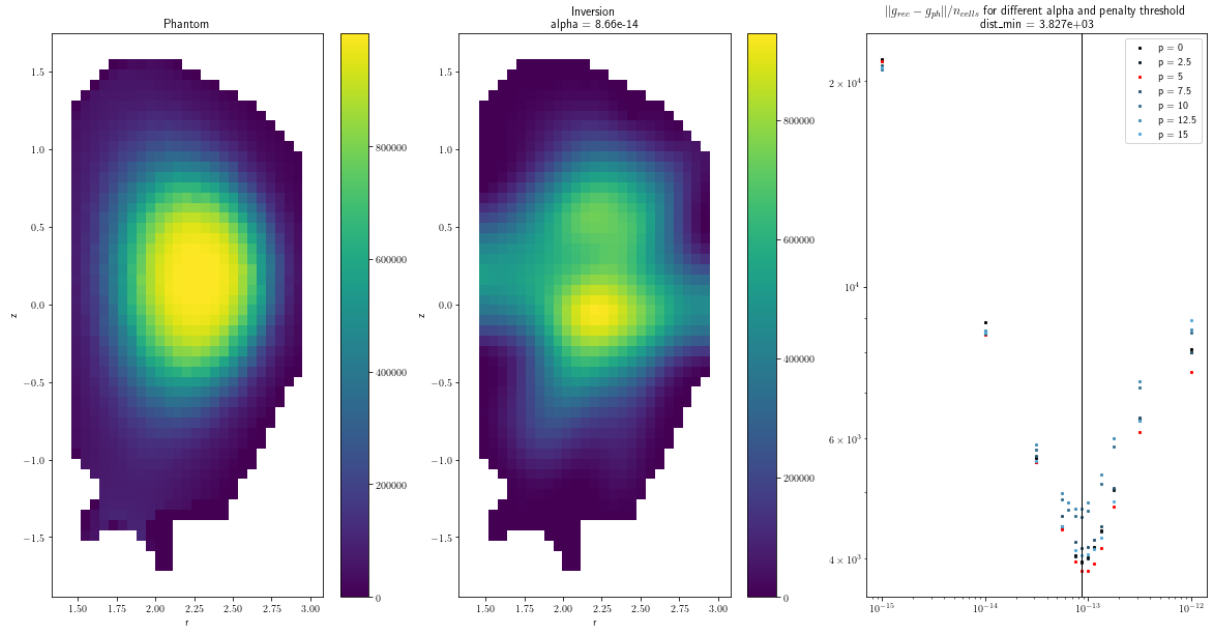Figure 18: Reconstruction with a finer mesh (mesh 4)

Figure 19: Reconstruction with the finest mesh (mesh 5)

From these pictures, two conclusions can be drawn :

- Finer is the mesh, better is the reconstruction (from the point of view of the distance from the phantom);

- Finer is the mesh, lower the penalty threshold should be. There's an exception for mesh 2 with a penalty threshold of 10% where 15% should be expected, but since the minimum distance is almost the same for every penalty threshold, it's not a major concern.

For the following tests, the finest mesh will be used since it provides better results. A finer mesh were not tested due to computation power limitations, but better results could have been expected. Moreover, when the second order regularisation is used, a penalty threshold of 5% will be applied.

10 Test emitters

The aim of this work is to determine what is the best setup for the bolometry in DTT. In order to test the different setups, some emitters are defined. Since a setup could provide a good reconstruction on a specific emitter and bad ones on others, multiple setups need to be defined.

These are arbitrary emitters. They are defined as function of the toroidal coordinate in order to be consistent with the magnetic field of the tokamak provided in an EFIT file. There are 3 main emitters representing possible emissivity fields (see figure 20). The number of different emitter is kept low since every reconstruction takes time (observation phase, then reconstruction phase, both can be long and require to be repeated multiple times).

All these arbitrary emitters are independent of the wavelength. These emitters shapes can be found in the X-ray range, the UV range or even the visible range. In the setup analysis, the wavelength doesn't matter, the emitter reflects what a sensor see. In a latter analysis 13, the wavelength could matter since realistic sensors are simulated, in this case, the multi-wavelength emitter is divided in parts. Each part corresponds to a wavelength range. It's like filters are applied to the emitters. Then, for each part, wavelength independent analyses could be carried on, like in this section.

The emitter "DTT_large" or just called "large" is defined as a Gaussian in the toroidal coordinate space :

$$\varepsilon\left(\psi_{axis}\right) = 10^6 \times \exp\left(-\frac{\psi_{axis}^2}{0.4}\right) \tag{25}$$

with ψ_{axis} the distance $\psi_n\left(r, z\right)$ from the magnetic axis where ψ_n is the normalised toroidal coordinate.

The second emitter "DTT_half_halo2" or "banana" is defined as :

$$\varepsilon\left(\psi_{axis}, \theta\right) = 10^6 \times \exp\left(-\frac{\left(\psi_{axis} - 0.7\right)^2}{0.025} - \left(\frac{\theta}{70}\right)^2\right) \tag{26}$$

The third main emitter is more realistic since it's the total emission (all wavelength are included) coming from a SOLPS output from a simulation introducing neon seeding in order to detach the divertor. This emitter is also really different from the previous ones since it is located only in the divertor region (below the X-point) and is really small : only two thin lines emit light from the X-point to the targets. It is called "SOLPS emitter"
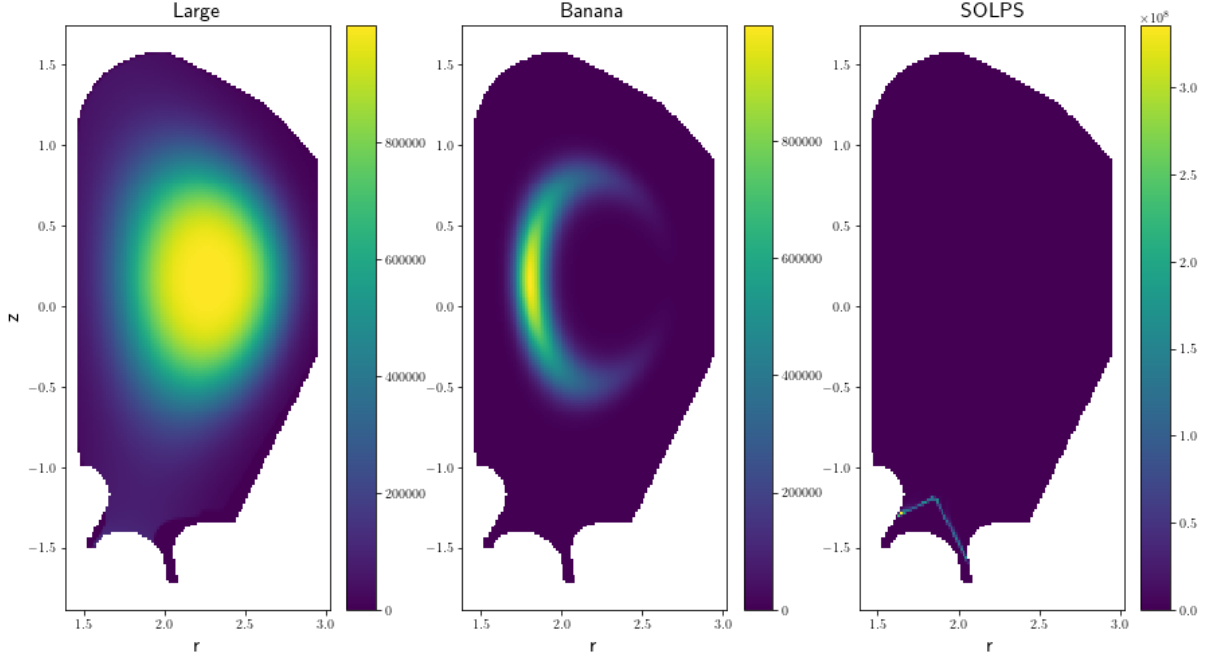

Figure 20: The 3 main emitters

Then there are variations with the SOLPS emitter. This emitter does not feature core plasma since SOLPS simulates only scrape of layer plasma, so a combination between the large emitter and the SOLPS one were made in order to assess the impact of core plasma on the reconstruction process of plasma below the X-point (presented later in section 12.2). Names of such emitter are "DTT_fullSOLPSxxx" with "xxx" replaced by a value which correspond to a factor in the definition. For example if "xxx" is "005" :

$$\varepsilon_{fullSOPLS05}\left(d_{axis}\right) = 0.05 \times 10^9 \times \exp\left(-\frac{d_{axis}^2}{0.4}\right) + \varepsilon_{SOLPS}\left(r, z\right) \tag{27}$$

The main factor before the large emitter is 10^9 because this value is really close to the maximum emissivity of the SOLPS emitter.

3 of these full SOLPS emitters are presented figure 21.
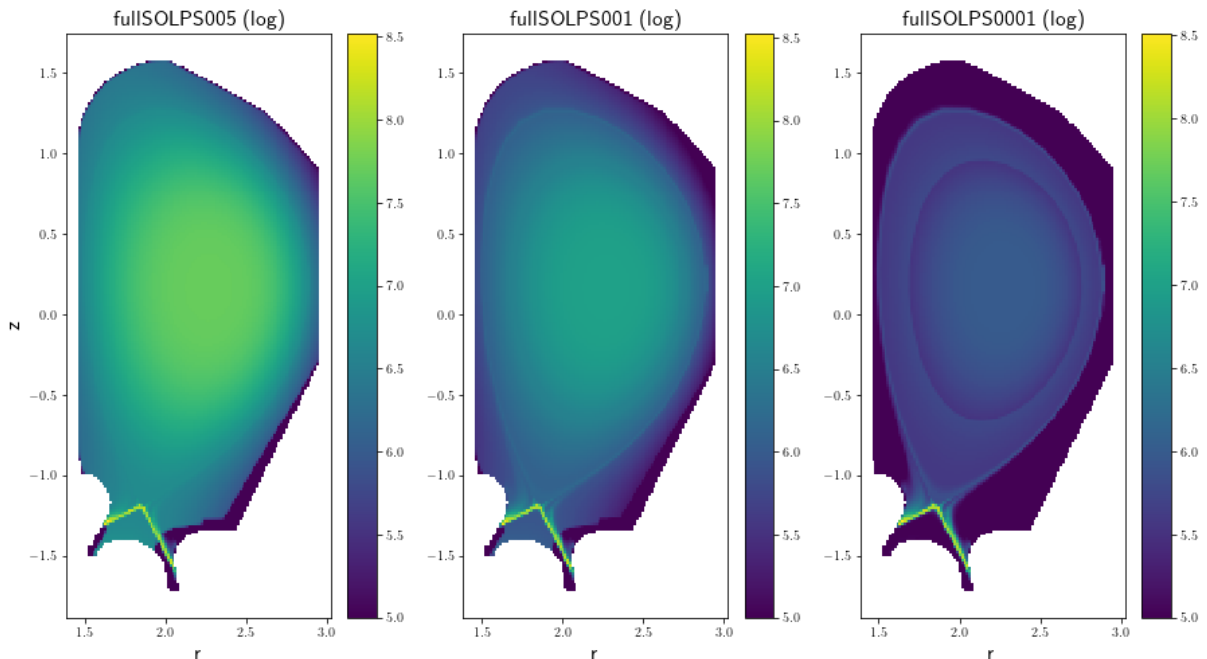

Figure 21: 3 fullSOLPS emitters (Attention, it's a log scale)

So to assess the effectiveness of a setup, 6 emitters are used : large, banana, SOLPS, fullSOLPS005, fullSOLPS001, fullSOLPS0001.

11 Setup analysis

The core of this work was carried out sequentially, first by testing a bunch of different ideas, then taking the best setups and introducing small variations on it. Names of the setups are "DTT_base" or "DTT_virtualxx" with "xx" being a number. For sake of simplicity, setups will only be called "base" or called by their number. When "xx" is written as "X_x", it means than the setup is the x-th variation of the number "X".

Setups are tests with the 6 emitters presented in section 10. The resulting distance from the phantom computed with Odstrčil reconstruction are presented in table 1. In order to determine the best setup, ranking is created :

1. a coefficient is attributed to each emitter c_e :

   - 1 for the 3 firsts emitters, since they are really different, their importance in the ranking is similar;
   - 1/3 for the 3 emitters which are a combination of the SOLPS emitter and the large emitter. These emitters are similar between them with respect to the 3 firsts, so the total weight of their contribution is the same than one of the 3 firsts emitters.

This current set of coefficient is imagined in order to obtain a setup good for core and divertor plasma reconstructions (large and banana emitters are focused on the core while SOLPS and fullSOLPS emitters are focused on the divertor area). However, by changing the value of the coefficients, it might possible to select a setup good for core reconstructions only, or divertor reconstructions only.

2. For each emitter e, the logarithm of the distance is ranked on a scale from 0 (smallest distance) to 1 (largest distance) taking into account all setups s : $d^s_{e,ranked} = \dfrac{\log\left(d^s_e\right) - \log\left(d^s_{e,min}\right)}{\log\left(d^s_{e,max}\right) - \log\left(d^s_{e,min}\right)}$. The logarithm of the distance is used because the distance ranges on several order of magnitudes. If a setup provides very bad results, the effect on a scale linear with the distance is to stack the good results at the top of the scale without much differentiation. The use of the logarithm of the distance permit to differentiate well good results when there are very bad results for an other setup. It also works in the opposite (if there is one good results when all the other ones are bad).

3. The mark is attributed to each setup as $m_s = \dfrac{\sum\limits_e c_e d^s_{e,ranked}}{\sum\limits_e c_e}$. This mark permit to rank the setups from 0 (best setup) to 1 (worst one).

In the following paragraphs, the setups compared are presented, the motivations for the positioning of the bolometers and the distribution of LoS are explained.

The first setup, the base setup (figure 22) is the starting point of this work. It is interesting to remark that some zones of the chamber aren't covered by any LoS. Some zones are covered by LoS which don't cross. If a light is emitted where LoS don't cross, the reconstruction algorithm "knows" that some light is emitted in this zone, but can't position it. So an homogeneous emissivity field will be reconstruct in this zone, which is not the result expected from the tomography.

From top to bottom, the number of LoS per bolometer is : 24, 24, 32, 16.

These peculiarities of this setup explain why it provides the worst results.

The goal of the setup 3 (figure 23) is to get the bolometers as close as possible to the plasma and provide a similar number of LoS by degree (so there are 8 missing LoS with respect to the maximum number). Consequently, the coverage is pretty homogeneous, no zone is left without LoS and the zones where LoS don't cross are little. This setup provides pretty good reconstructions with respect to the base setup. The number of LoS per bolometer is 20, 24, 36, 8.

The setup 5 (figure 24) is based on the idea that the divertor should require a denser coverage since for the setup 3, the 2nd order regularisation for the SOLPS emitter didn't provide satisfying results. So LoS are added between existing ones and a new bolometer is added (the cyan one), looking toward the divertor. The number of LoS per bolometer (top to bottom) is : 18, 27, 6, 40, 5. This setup provides better reconstructions than the previous one.

The setup 6 (figure 25) was imagined by Silvia Palomba. The main idea is to multiply the number of sources, "splitting" the bolometers (there is not enough space in the ports of the black and green bolometer to "split" them). The main effect is to avoid that any space inside the limiter be empty of LoS crossroads. This setup provides even better reconstructions than previous setups.

The number of LoS is 21, 12, 12, 17, 18, 16.

The first variation on the setup 6 (figure 26) aims at reducing the density of LoS in the green bolometer, while increasing it in others bolometers. Since the étendues of LoS coming from the green bolometer are the shortest, placing source of LoS in other bolometers will increase the average sensitivity : If a LoS is longer, it passes through more cells, so has an influence on more cells, so the total sensitivity is higher. The number of LoS is then 22, 14, 14, 19, 20, 7. Nevertheless the reconstructions were not better.

The second variation on the setup 6 (figure 27) focus on red and blue bolometers. When a pair is considered, the top bolometer look partially toward the divertor but not the bottom one. So the idea leading to this setup is to shift some of the LoS coming from bolometers not looking toward the divertor

to bolometers which do look at it. So the number of LoS becomes 21, 15, 9, 20, 15, 16. This setup provides reconstructions which are sometimes better than the original setup 6 (for the large emitter and 2 of the fullSOLPS), so it gets a better mark and is the best setup according to the notation system.

The setup 6_3 (figure 28) is based on 6_2 and adds more LoS in the green bolometer (1 LoS coming from each bolometer) to increase its density, since the decrease seen with setup 6 to 6_1 gave bad results, an increase might give good results. However it was not the case.

The fourth and fifth variations of the setup 6 (figures 29 and 30) aims at varying the number of LoS shifted from bottom to top bolometers. Their mark is below the one obtained by the setup 6_2. The most surprising is the variation of the results. It could be expected that a small variation in the setup would lead to a small one in the results, but it doesn't seem to be the case. No explication was found to justify this.

Setup 7 (figure 31) was designed such as provide the same improvement to setup 6 as setup 5 was for setup 3. Which means densify the LoS around the divertor by placing new LoS looking to the divertor in between existing ones. However, this change did not provide better reconstructions but worst ones. The variation 7_1 (figure 32) aims the same goal but keeping the initial number of LoS coming from the green bolometer. Reconstructions are worst.

Setup 8 (figure 33) is similar to 6_2, it aims at providing a density of LoS more homogeneous between the bolometers. The reconstructions are good, but not better than those of the setup 6_2.

Since dividing LoS source in pairs gave good results, the setup 9 (figure 34) aims at dividing the LoS sources again. Red bolometers becomes 3 and blue ones, 4. However the results were not better than the third setup.

Setup 10 (figure 35) continues on this idea, but directing the bolometers in others directions. This setup didn't provide better results.

The main difference between the 2 last setups and setups 6 is that there are more LoS crossroads, which should be an improvement, however they are mostly located outside the limiter, so there are useless.

Finally the best setup is the 6_2 according to the ranking system. Some tests on indicators were done in order to verify if the maximisation or the minimisation of a statistic may reflect the results of the ranking, however it did not provide any interesting results. The statistics were the average total sensitivity, the average number of LoS crossroads per cell, and the relative standard deviation of each one of these statistics.

	Large	Banana	SOLPS	fullSOLPS005	fullSOLPS001	fullSOLPS0001	Final mark	Rank
base	7,67E+03	3,40E+03	1,20E+05	4,39E+05	1,26E+05	4,39E+05	0,89	14
virtual3	6,41E+03	3,20E+03	1,01E+05	3,09E+05	1,21E+05	9,18E+04	0,41	7
virtual5	4,57E+03	3,21E+03	1,04E+05	2,75E+05	1,14E+05	9,39E+04	0,26	3
virtual6	5,37E+03	2,79E+03	9,99E+04	3,06E+05	1,13E+05	7,55E+04	0,17	2
virtual6_1	5,69E+03	3,65E+03	1,07E+05	3,08E+05	1,21E+05	1,03E+05	0,53	9
virtual6_2	4,16E+03	3,28E+03	9,95E+04	2,39E+05	1,06E+05	9,97E+04	0,13	1
virtual6_3	5,52E+03	3,06E+03	1,13E+05	2,81E+05	1,08E+05	9,73E+04	0,40	6
virtual6_4	5,24E+03	3,41E+03	9,98E+04	2,91E+05	1,15E+05	8,28E+04	0,31	4
virtual6_5	6,21E+03	3,56E+03	1,16E+05	3,14E+05	1,20E+05	1,05E+05	0,66	13
virtual7	6,40E+03	3,56E+03	1,06E+05	3,65E+05	1,17E+05	9,61E+04	0,55	10
virtual7_1	7,08E+03	3,96E+03	1,01E+05	3,74E+05	1,25E+05	9,44E+04	0,64	12
virtual8	5,24E+03	3,26E+03	1,08E+05	2,83E+05	1,10E+05	9,27E+04	0,36	5
virtual9	6,01E+03	3,76E+03	1,06E+05	2,73E+05	1,17E+05	9,07E+04	0,52	8
virtual10	7,26E+03	3,40E+03	1,09E+05	3,36E+05	1,16E+05	7,63E+04	0,57	11

Table 1: The distance from the phantom for each couple setup/emitter. The colors shows if the distance is good (green) or bad (red) for each emitter; middle values are white. The 3 best setups are highlighted. In this table raw distance cannot be compared between emitters for a same setup since this distance is highly emitter-dependent. The only pertinent comparison of euclidean distance is between setups for a same emitter.
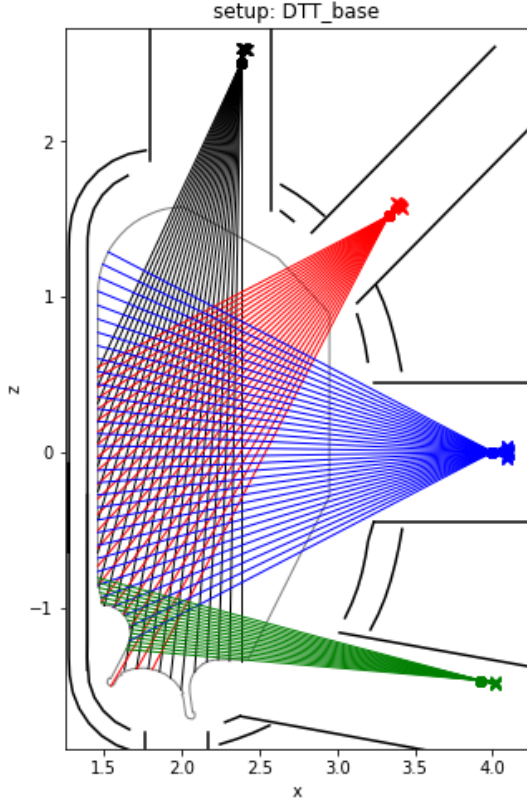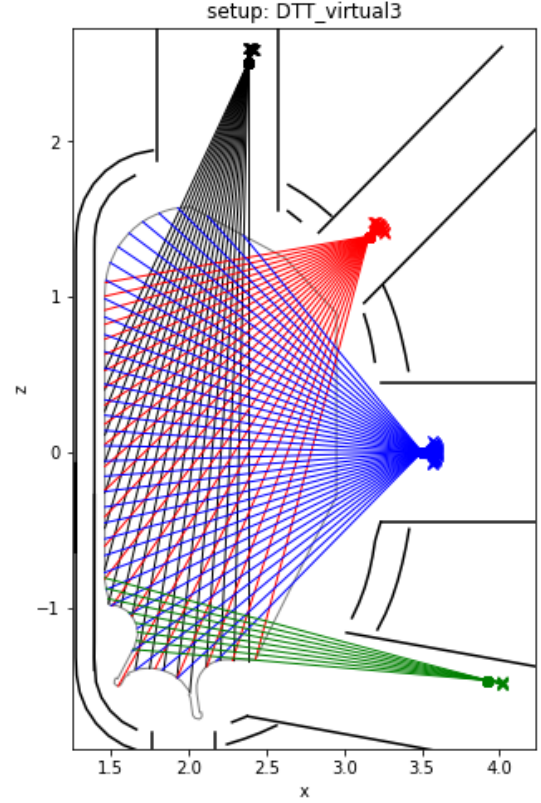

Figure 22: Base setup
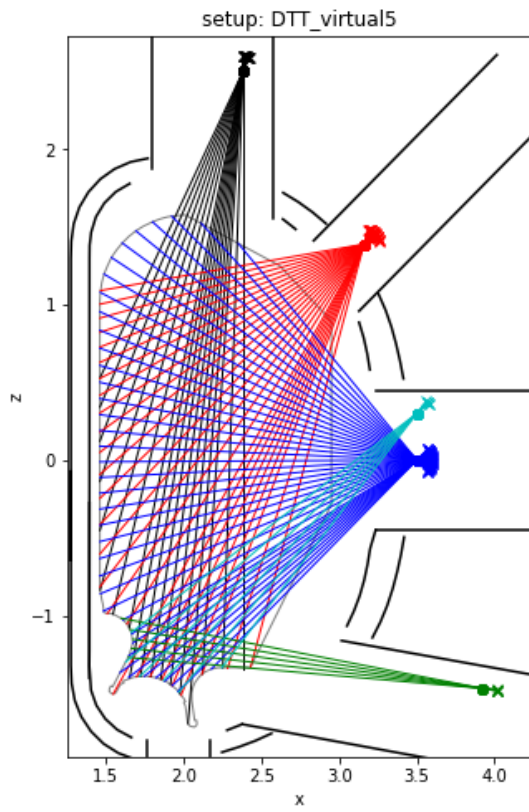

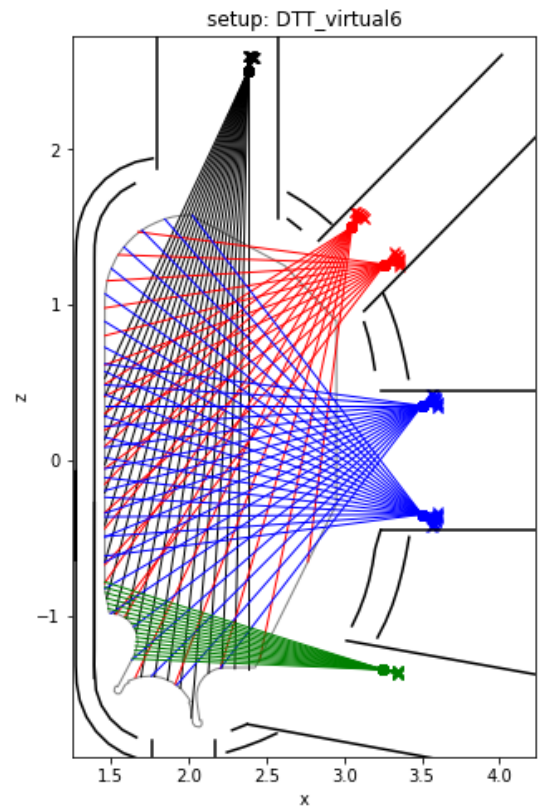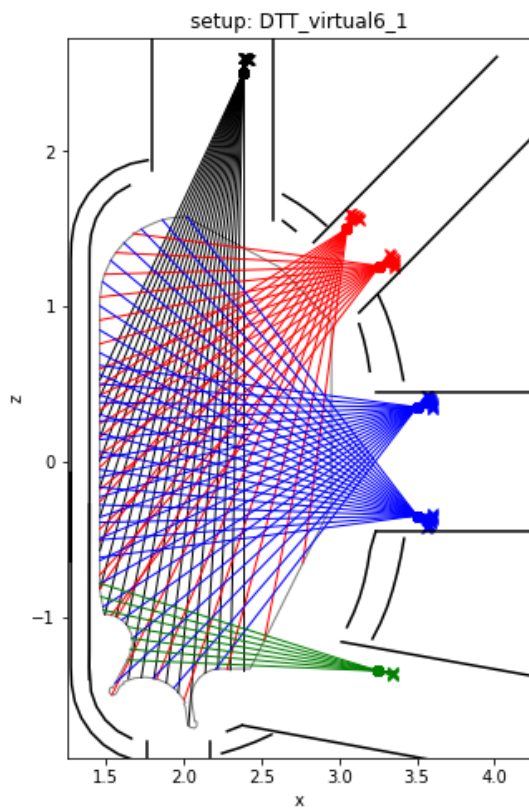
Figure 23: Setup 3

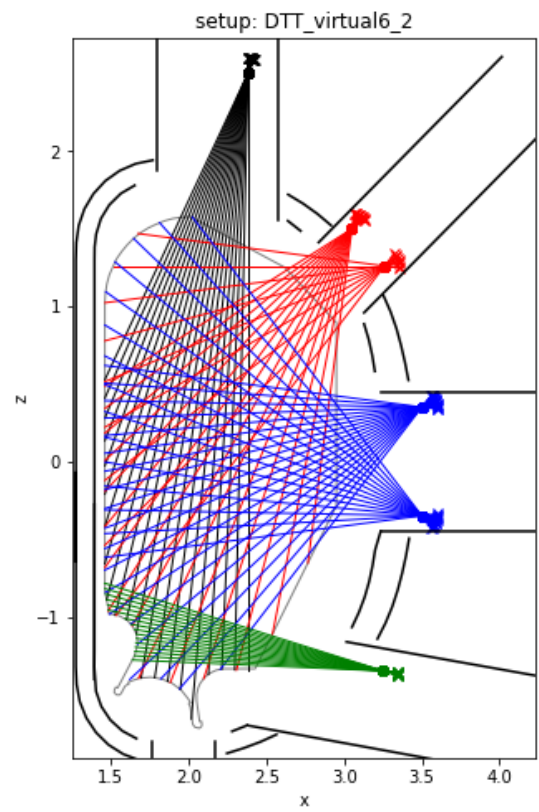Figure 24: Setup 5

Figure 25: Setup 6
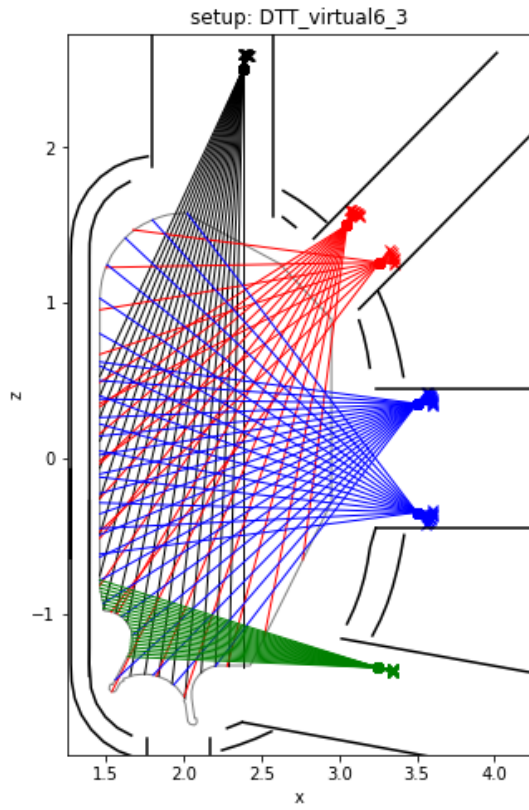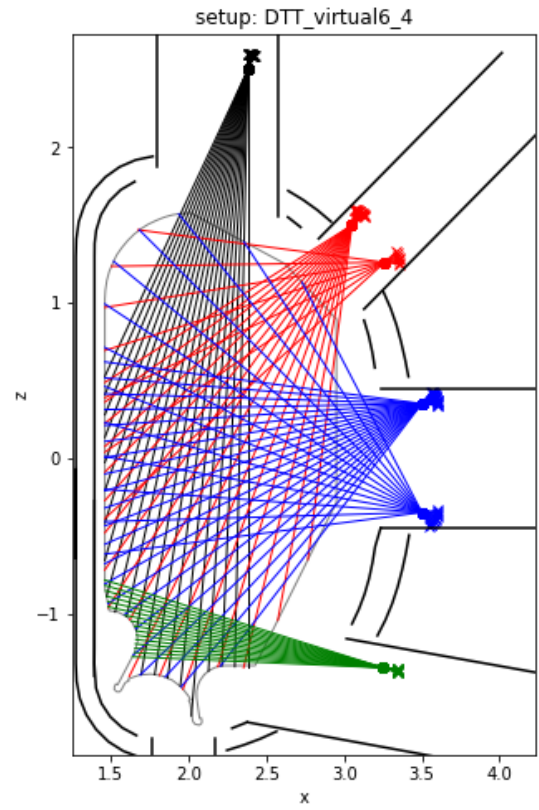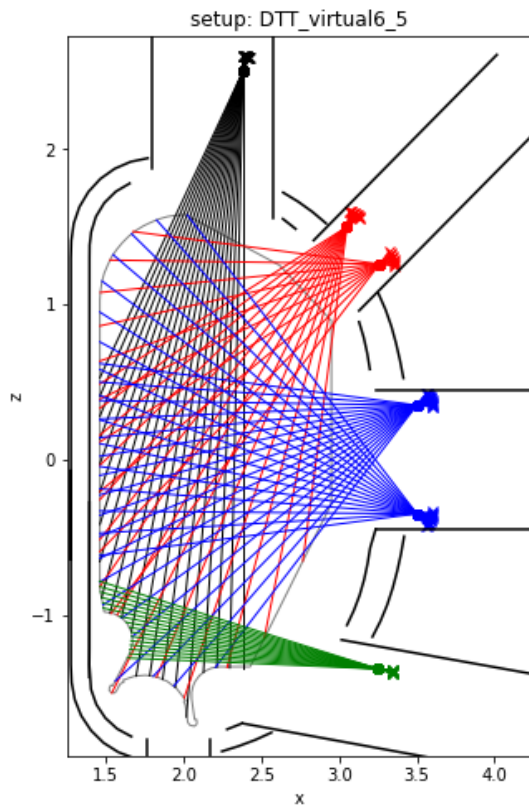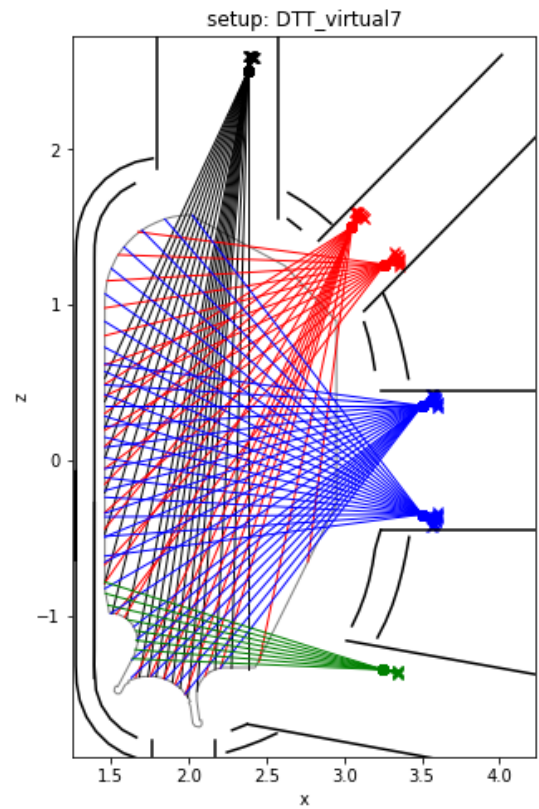

Figure 26: Setup 6_1
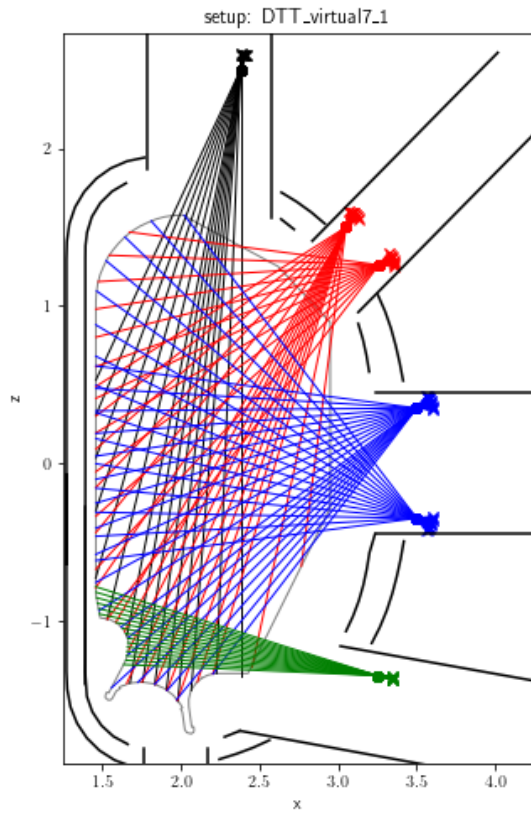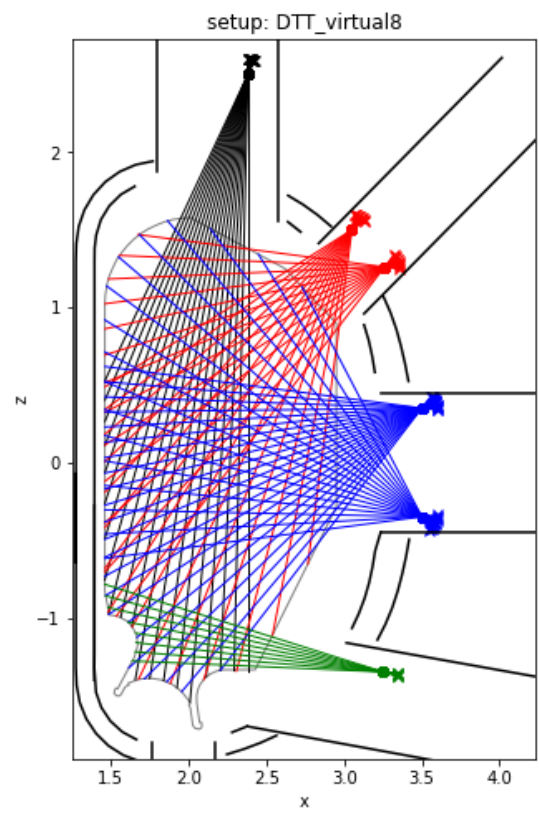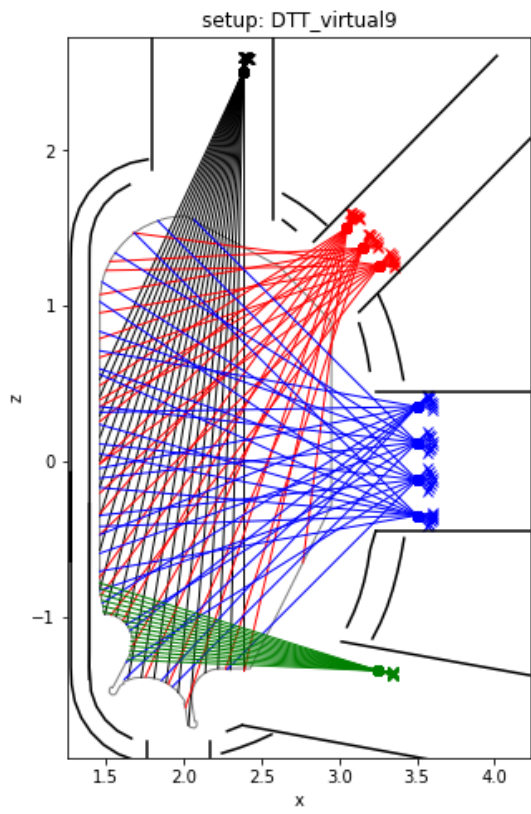

Figure 27: Setup 6_2

setup: DTT_virtual6_3

setup: DTT_virtual6_4

Figure 28: Setup 6_3

Figure 29: Setup 6_4

setup: DTT_virtual6_5

setup: DTT_virtual7

Figure 30: Setup 6_5

Figure 31: Setup 7

30

setup: DTT_virtual7_1

Figure 32: Setup 7_1

setup: DTT_virtual8

Figure 33: Setup 8

setup: DTT_virtual9

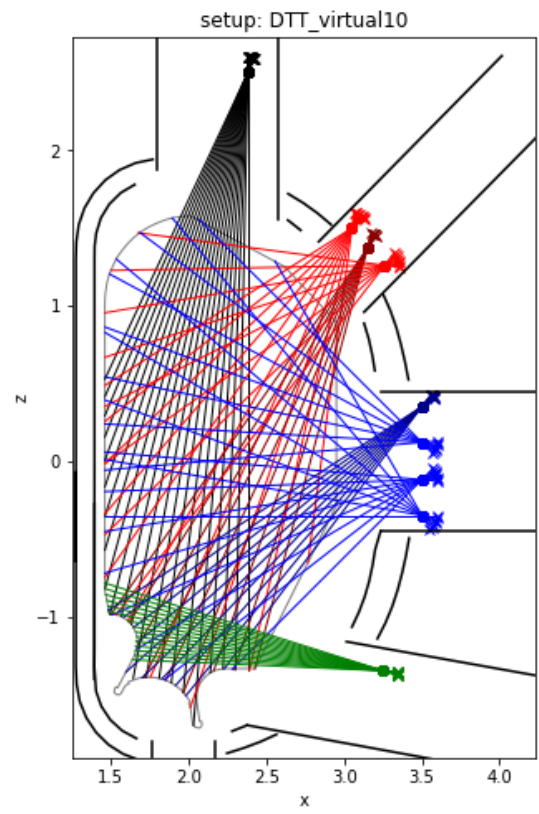Figure 34: Setup 9

setup: DTT_virtual10

Figure 35: Setup 10

12   Other analyses

12.1   Comparison of the reconstruction algorithms

Reconstruction algorithms were presented in section 4. According to the bibliography, MFI is widely used as the 2nd order regularisation in experimental conditions. It is for these reason that the other reconstruction algorithms are not considered for this work. The Anton's regularisation is not considered since the Odstrčil's regularisation is an improvement of this method.

In order to compare these algorithms, analyses of the setup 6_2 were done twice, once with the Odstrčil's regularisation, once with the 2nd order regularisation. The inversions are presented figure 36 to 41. In these pictures, the color bar for the phantom emitter is different from the reconstructions one since there might be a high gap between the maximal values of the reconstructed emitter and the phantom emitter. However the color bars of the reconstructions is the same (for each emitter) to permit a easy comparison between reconstructions.

From the point of view of the distance, these methods provide similar results. The distance is a bit lower for the 2nd order regularisation in cases of the large and banana emitters, and the trend is inverted in cases of the SOLPS and fullSOLPS emitters. This statistic will not help to choose one of the algorithm.

A deeper analysis of the reconstructions is necessary. Considering the banana emitter (figure 37), the results are almost the same, the main difference the maximum emission which is a bit smaller for the Odstrčil's regularisation. For the large emitter (figure 36), the shape of the reconstructions are similar, but a difference can be seen. Indeed the 2nd order regularisation provide a smoother reconstruction while the result provided by the MFI shows artifacts of the LoS, lines can be guessed. This smoothness of the 2nd order regularisation is normal since this is the aim of this reconstruction (minimizing the Laplacian is maximising the smoothness). These small differences between the 2nd order regularisation reconstructions and Odstrčil ones justify the slight difference in the distance.

The reconstructions of the SOLPS emitter are also similar (figure 38), but there are important differences. The 2nd order regularisation reconstruction shows multiple artifacts of low emissivity in the core region and the emission in the divertor doesn't cover the whole divertor area. Finally, as for the large emitter, the reconstruction is smoother than the one obtained with MFI. In this case the smooth result is not wished since the phantom shows a really thin and sharp emission. The emission in the divertor is poorly covered by the LoS, so Odstrčil's reconstruction benefit the bias of the flux in order to place emission in this region.

Concerning the fullSOLPS0001 emitter (figure 41), both reconstructions place a large emission in the divertor region. None is close to the real emission, but according to the analyses section 12.2, it's the best that can be expected. The artifacts are emitting more and are numerous in the 2nd order regularisation reconstruction.

For fullSOLPS001 (figure 40), both reconstructions overestimate the power emitted in the core region, but it's noticeable that the MFI reconstruction still places an emission source in the divertor region.

Finally, for fullSOLPS005 (figure 39), reconstructions are similar and the same conclusions than for the large emitter can be drawn. None of the reconstructions place an emission in the divertor area.

Considering this analysis, both reconstruction method are used in the report, 2nd order regularisation provides better result for smooth emitters like the large one, but the Odstrčil one permit to obtain further details, especially in the divertor area. Other analyses in this report will show that both reconstruction methods are complementary.
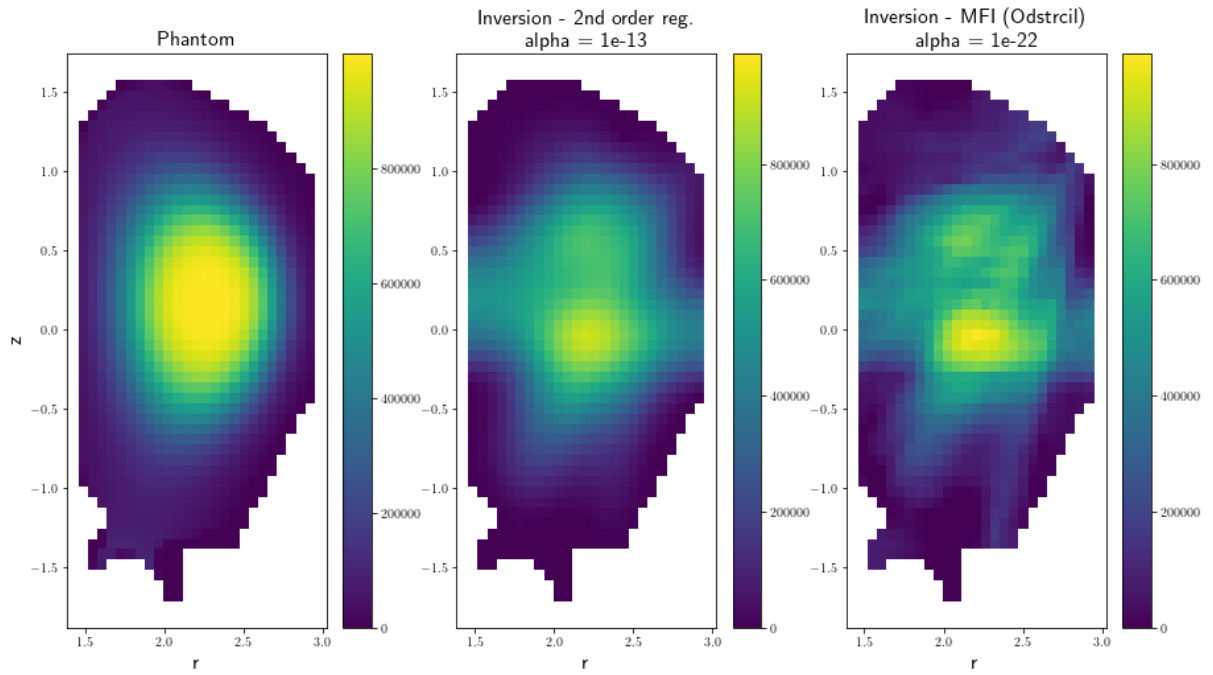
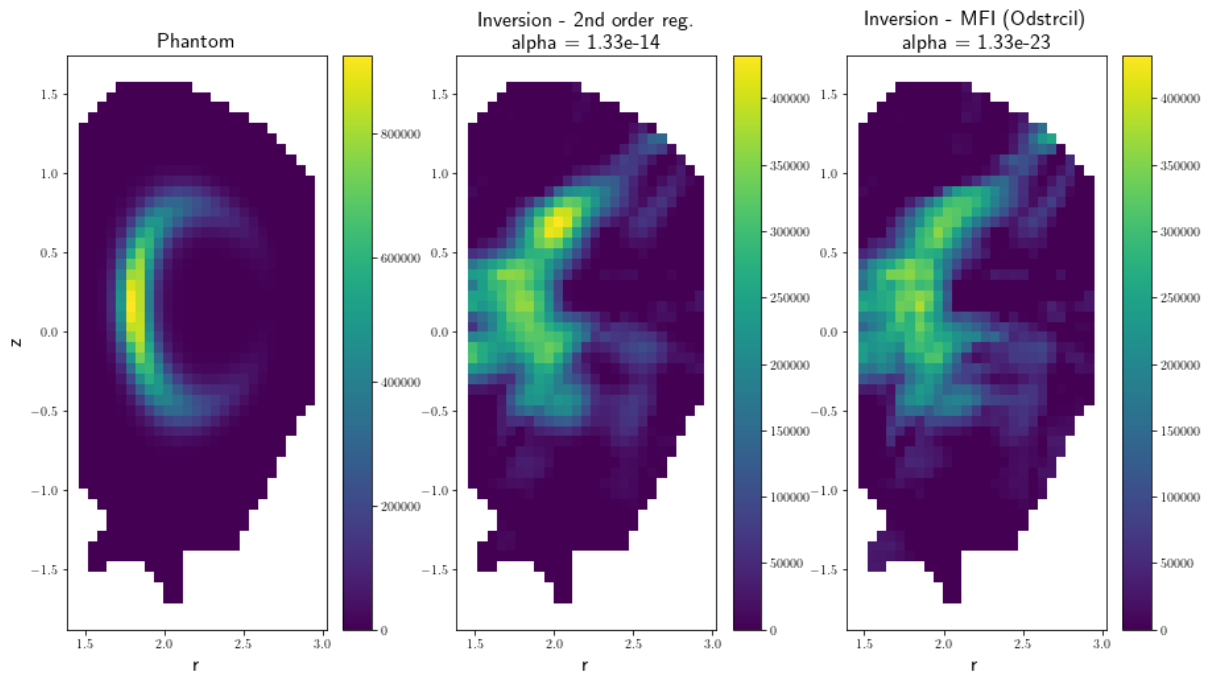Figure 36: Comparison of the reconstructions for the large emitter

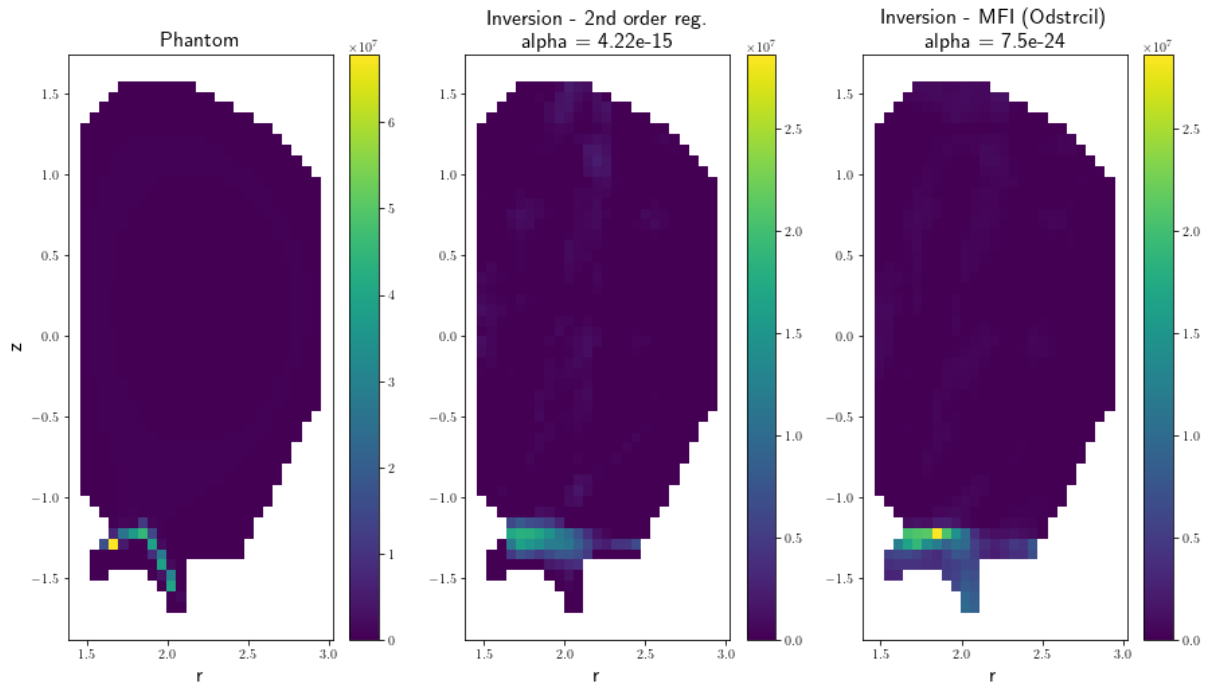Figure 37: Comparison of the reconstructions for the banana emitter

Figure 38: Comparison of the reconstructions for the SOLPS emitter
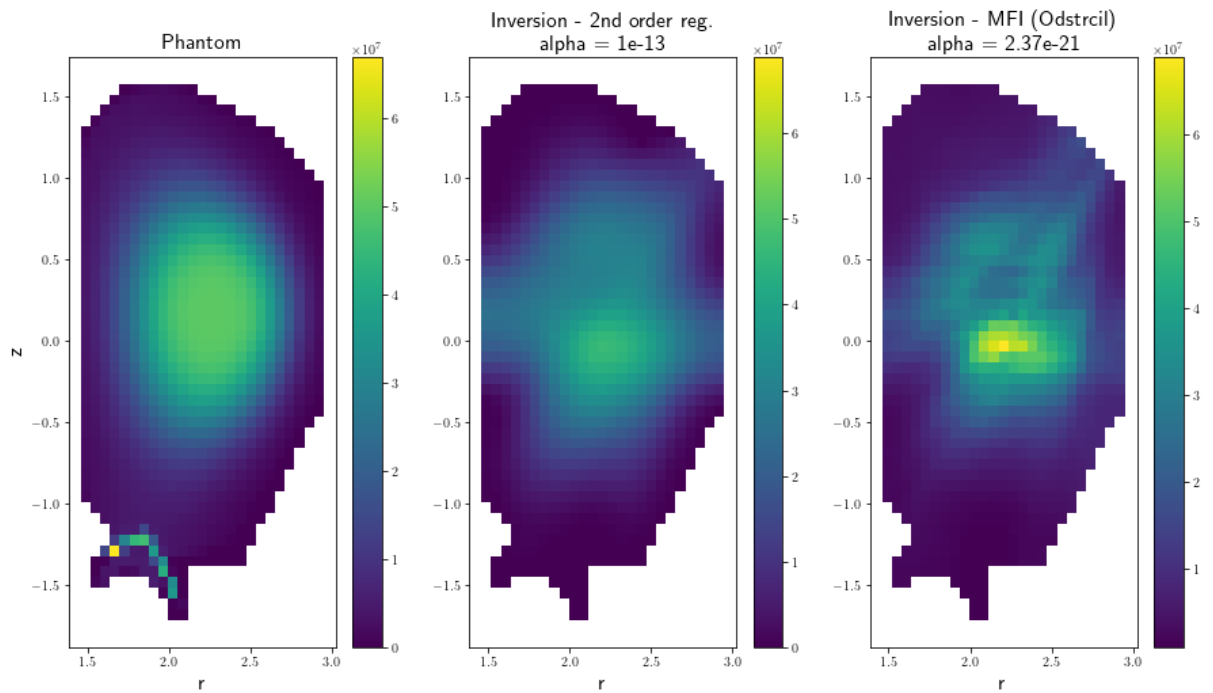

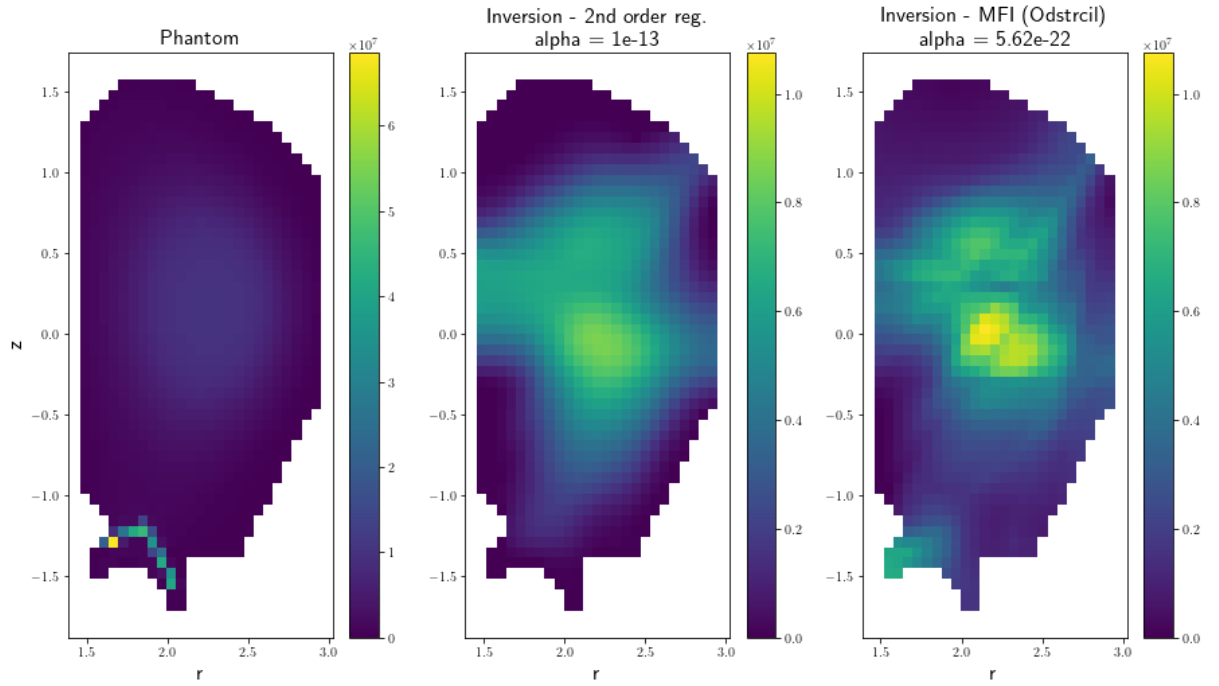Figure 39: Comparison of the reconstructions for the fullSOLPS005 emitter

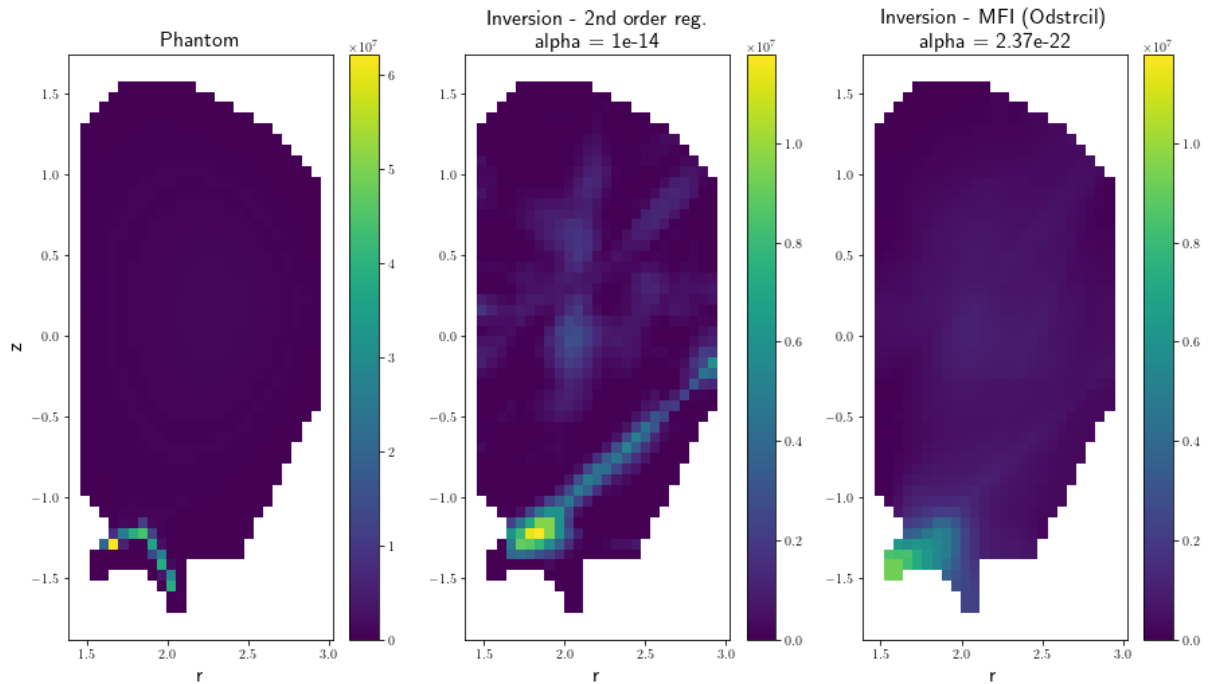Figure 40: Comparison of the reconstructions for the fullSOLPS001 emitter

Figure 41: Comparison of the reconstructions for the fullSOLPS0001 emitter

12.2 Perturbations on the SOLPS emitter

In this section, core emitter will refer to the light emitted by core plasma, inside the separatrix. Divertor emitter will refer to the light emitted by private plasma, below the X-point.

The tests on the SOLPS plasma lack a bit of reality since no core plasma is simulated by SOLPS and so, there is no core emitter in the SOLPS emitter. It is possible to suppose that a core emitter would be negligible with respect to the divertor emitter since the latter peaks at $10^9\,\mathrm{W/m^3}$. However since the section covered by the core emitter is really wide and the section covered by the divertor emitter is very thin, the total power emitted by the core plasma might be larger than the one emitted by the private plasma (21.5 MW). The total power is computed taking into account of the volume of each cell. The total power emitted by core plasma is factor $\times\,3200\,\mathrm{MW}$ where "factor" is the one in fullSOLPSxxx. These values are obtained directly from an analysis of emitters and do not reflect real power which can be measured in DTT.

These tests aim at verifying if it is possible to reconstruct the SOLPS plasma when there is a core emitter. They were carried during the determination of the best setup with the setup 3. Many plasma were created for this test, all of the type fullSOLPS, where the factors are : 0.5, 0.2, 0.1, 0.01, 0.001, 0.0001, but just a selection is presented. The reader can notice that the power shown on phantom plasma doesn't peak to $10^9\,\mathrm{W/m^3}$, this is because the value of a cell is computed as an average of the values covered by this cell (with a Monte-Carlo process) and not the central value or maximum value. In this case, the section covered by the SOLPS emitter is very thin, so the maximum power in the plots is below $10^9\,\mathrm{W/m^3}$.

The observations are available figures 42 to 45, and the Odstrčil reconstructions on the figures 46 to 45. The reconstruction plots show that the shape of the divertor emitter is in the best case (no perturbation) poorly reconstructed. In the worst cases (important perturbation), the divertor emitter is not reconstructed at all.
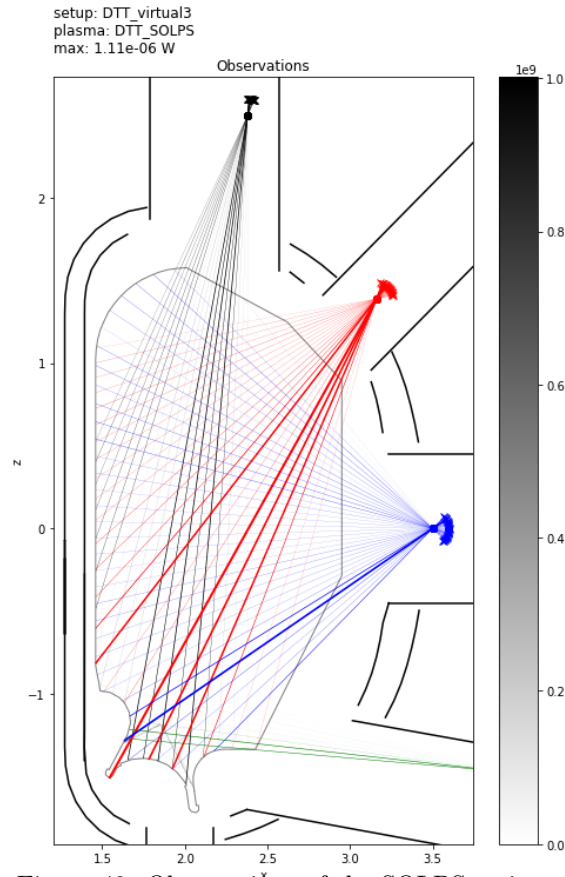
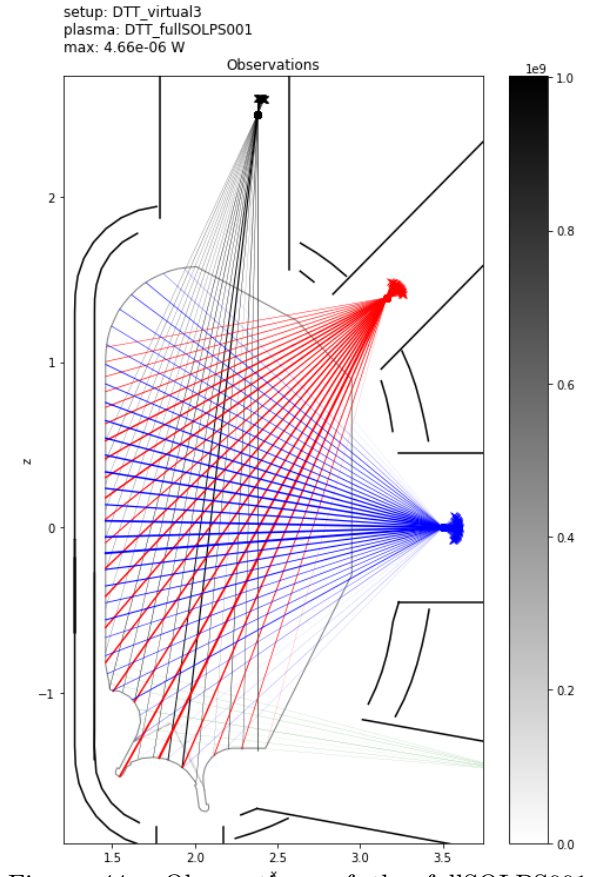Figure 42: Observations of the SOLPS emitter

Figure 44: Observations of the fullSOLPS001 emitter, some sensors pointing toward the divertor catch still more light than the others sensors
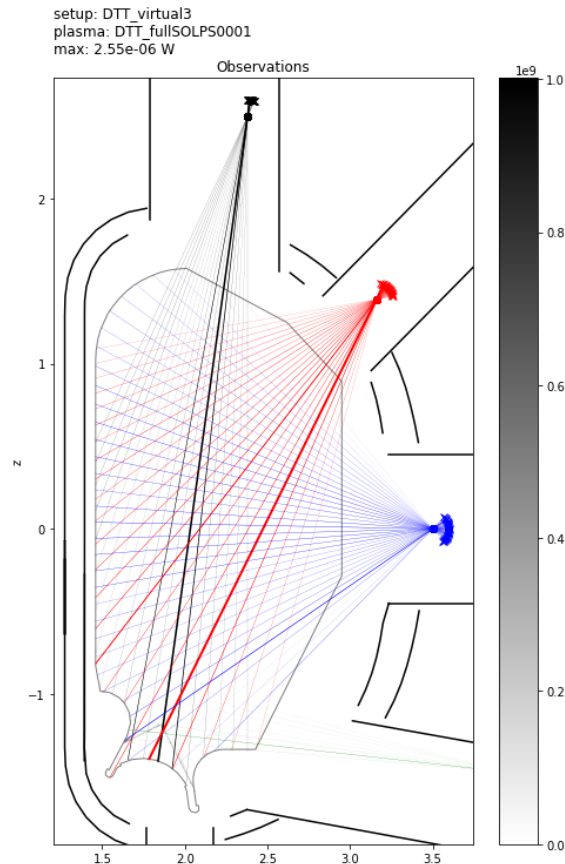

Figure 43: Observations of the fullSOLPS0001 emitter, the sensors pointing toward the divertor catch still more light than the others sensors
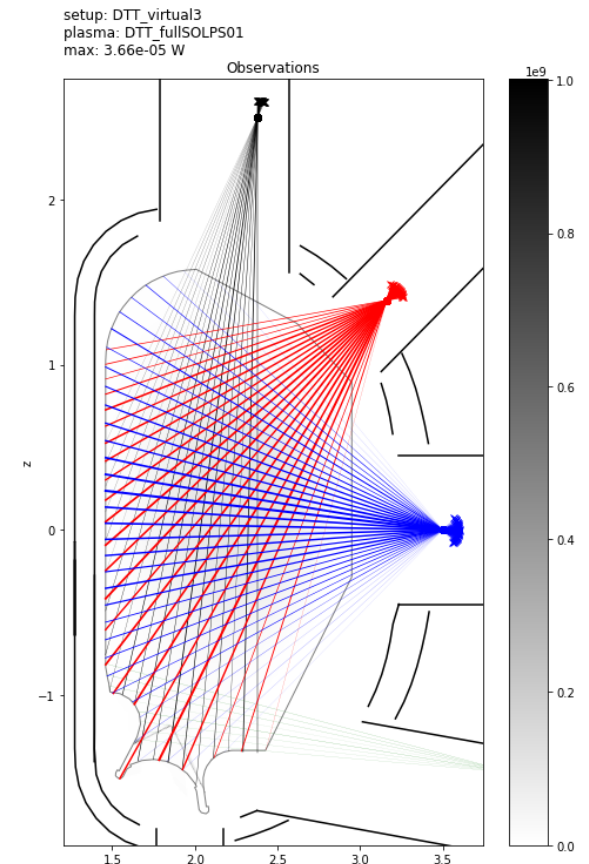

Figure 45: Observations of the fullSOLPS01 emitter, the excess of light seen by the sensors pointing toward the divertor is not notable

This phenomenon can be explained with the observations : on the observation of the SOLPS emitter (no perturbation), the sensors which receive most of the light are those pointing toward the divertor, or those pointing toward reflections on the walls. From the observation of fullSOLPS001, the sensors pointing toward the divertor receive some more light than the other sensors. Higher is the perturbation, lesser is the relative importance of the light received from the divertor as compared with the core. So it is understandable that the algorithm have hard time to "know" that light is coming from the divertor emitter, so the reconstruction of the divertor emitter is poorer. However the core emission seems correctly reconstructed at any time : the overall shape and maximal emission are preserved.

A simple criterion applicable to this experiment can be that emission is well detected in the divertor area when the total power in the divertor area is 1 order of magnitude higher that the total emission in the core area. This analysis, like the others is made with the best reconstruction parameter, meaning that a different reconstruction parameter might influence this criterion.
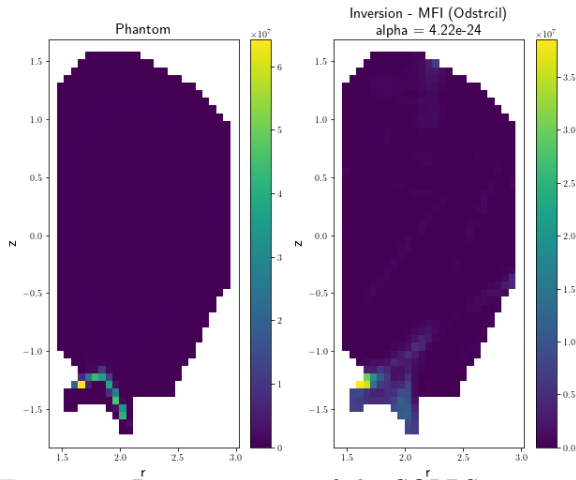

Figure 46: Reconstruction of the SOLPS emitter, the reconstruction is far from perfect, but it's the best which can be expected
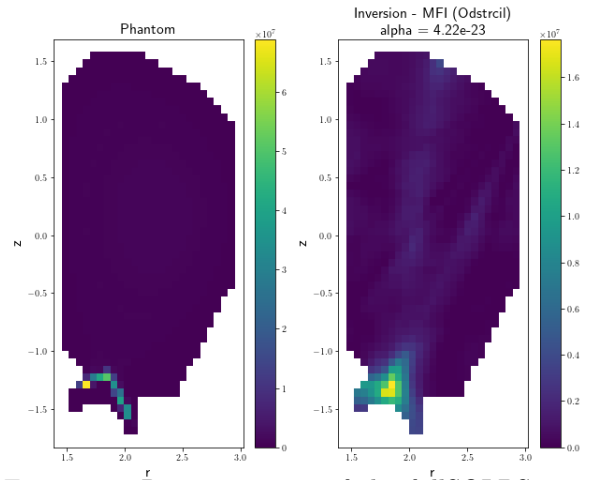

Figure 47: Reconstruction of the fullSOLPS0001 emitter, the reconstruction in the divertor area is not good
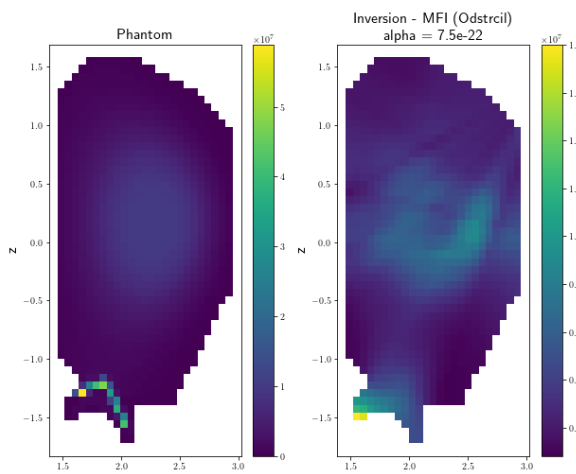

Figure 48: Reconstruction of the fullSOLPS001 emitter, but the reconstruction in the core area is not bad since the order of magnitudes are respected
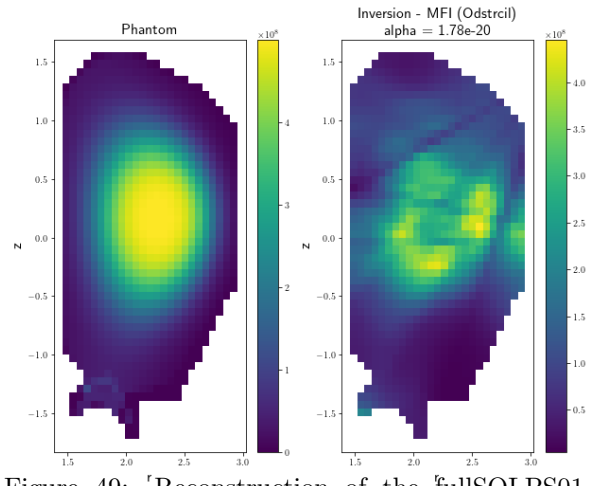

Figure 49: Reconstruction of the fullSOLPS01 emitter, there's almost no reconstruction of the divertor emission which is really weak, but the core emission is pretty well reconstructed (it keeps the overall shape and maximal emission)

13 Realistic emitter and "coloured" analysis

13.1 Electron and ions profiles

From now, all previous emitters were totally arbitrary, with few relations with what could be really seen in DTT. Since it's possible to input density profiles and temperature profiles to CHERAB, it could be possible to obtain a "realistic" emitter. An emitter coming from SOLPS simulation was already used, but with no or an arbitrary core light emission (SOLPS emitter, fullSOLPS emitters), so only a simulated core emission consistent with the SOLPS emitter is necessary.

So the Casiraghi *et al* 2021 publication [3] is the base of this core emitter, especially the profiles of ion and electron temperature, electron density and rotation coming from the figure 3 or 10 of the article.

However, since results from the SOLPS simulation include a region of the core, between

Figure 50: Profiles (in red) of electrons and ions temperature and electron density (figure 10 of [3])

the separatrix and $\rho_t \approx 0.8$, the value calculated depends both of the SOLPS simulation and Casiraghi's simulation and are linearly weighted with the distance. For example, for a quantity Q at the position $\rho = 0.95$, $Q_{0.95} = Q_{SOLPS} \times 75\% + Q_{core} \times 25\%$.

Some modifications were made to the core profile :

- At the separatrix, the electron density is increased by a factor 1.4 to ensure the continuity;

- Since deuterium density is not given in the paper, in CHERAB, this density is the same than electron density (in figures 51 and 53, only the part simulated by SOLPS differs);

- In the SOLPS simulation, neon is seeded in the tokamak in order to detach the divertor. Neon is not included in Casiraghi's simulation. So the density of minority neon ions is arbitrarily set to flat in the region not covered by the SOLPS simulation. For Ne^{10+}, they are set proportional to deuterium ions in this region.

These adaptations are necessary to provide a realistic output. Ensuring continuity in electron density will ensure continuity in light emission (since light emitted by excitation and recombination, the main phenomenon of emission in plasma, is proportional to electron density).

Deuterium density equals to electron density is a first approximation but is realistic since impurities in the plasma (neon in this case) are a minority (about 2 order of magnitude of difference between the densities of fully ionised deuterium and neon in the core region). So the number of electrons added by the neon ions can be considered as negligible.

Considering the flat density profile of neon ions in the core, this might be not realistic. Usually the density is set proportional to the main ion. However the quantity of the other neon ions in the core region should decrease with the temperature, however since their density is already low in the core region (see figure 54), their contribution to light emission is negligible, a flat profile is an acceptable first approximation.
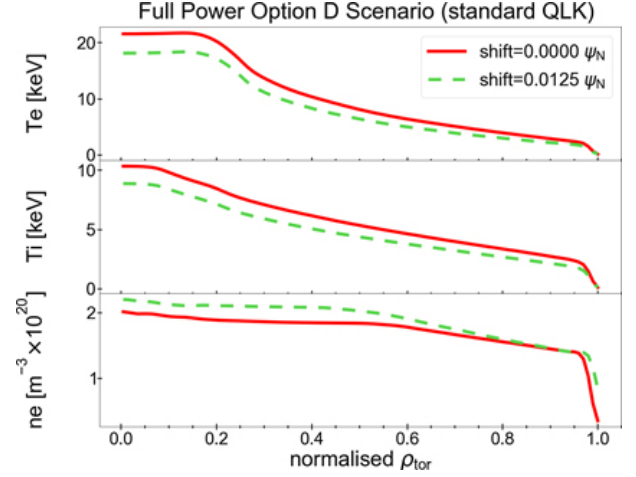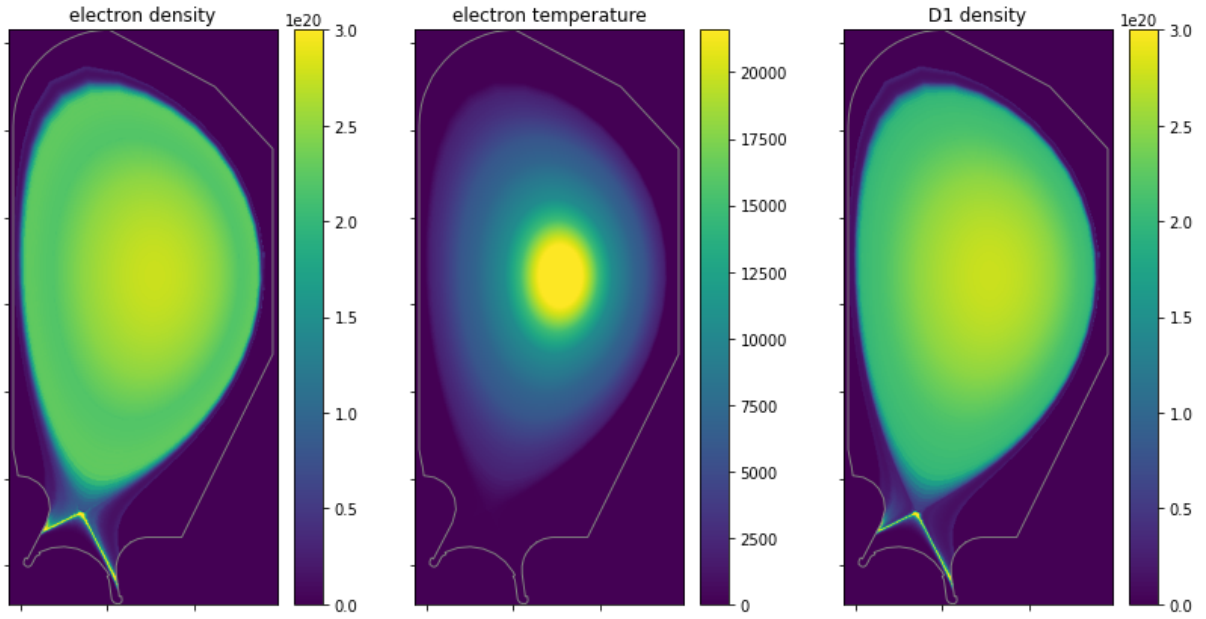
Figure 51: Electron density in m^{-3}, in the plot the values are limited to $3 \times 10^{20}\,m^{-3}$

Figure 52: Electron temperature in eV

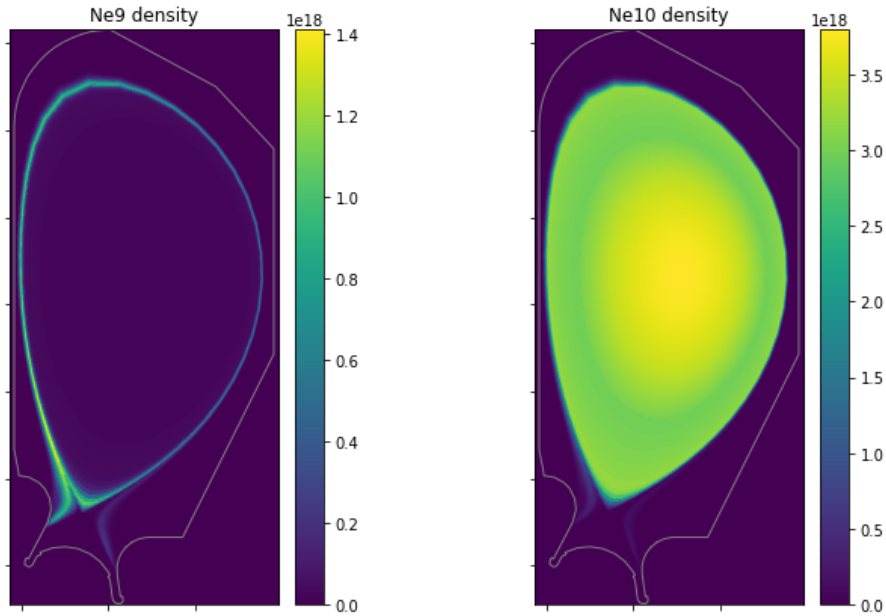Figure 53: D^+ density in m^{-3}, in the plot the values are limited to $3 \times 10^{20}\,m^{-3}$

Figure 54: Ne^{9+} density in m^{-3}

Figure 55: Ne^{10+} density in m^{-3}

13.2   Resulting emitters

There are 3 main domains which are analysed by bolometers, visible and near infrared (400 nm - 1000 nm), ultraviolet (10 nm - 400 nm) and X-ray (0.01 nm - 10 nm). CHERAB can differentiate the wavelength in the observations through the ray-tracing algorithm and thus includes modifications of the wavelength of a light ray through diffusion for example (coloured observations). However this process would require more computational power than an observation without differentiating wavelengths. Moreover, the current code version is optimized for non-coloured observations. For these reasons, another

process is used.

Instead of creating 3 different observers and 1 coloured emitter, the observer is still the same but there are 3 different emitters (associated to one domain each). For the emitter relative to the UV domain, it includes only the light which is emitted in the UV domain by the realistic emitter. The process is the same for the Visible-IR and X-ray related emitters. It's an approximation since it doesn't take into account the possibility of the light to shift from one domain to another, but since this phenomenon can be considered as negligible, the approximation is acceptable.

The resulting emitters show for X-ray that the light is emitted along the separatrix below the X-point (up to 10^7 W·m^{-3}). Light is emitted also in the center of the core region, but the maximum in the core region is about 4 times below the maximum in the divertor region. It could be interesting to have a wider SOLPS simulation in the SOL region since the emission is still important on the limit of the SOLPS mesh (more than 10^7 W·m^{-3} on the outer side). Concerning the UV region, light is emitted mostly below the X-point, along the separatrix. The light emitted elsewhere is negligible (4 orders of magnitude below for the core region with respect to the divertor region) with a little resurgence at the outer side of the limiter. For the visible-IR domain, light is mostly emitted at the strike points. Light emitted along the separatrix below the X-point is 2 order of magnitudes below, as some light emitted near the surface of the limiter. It might be possible that some light is emitted on a wider limiter surface, however the SOLPS mesh doesn't extent on all the limiter.
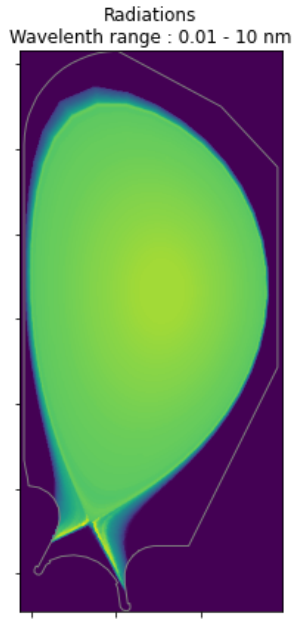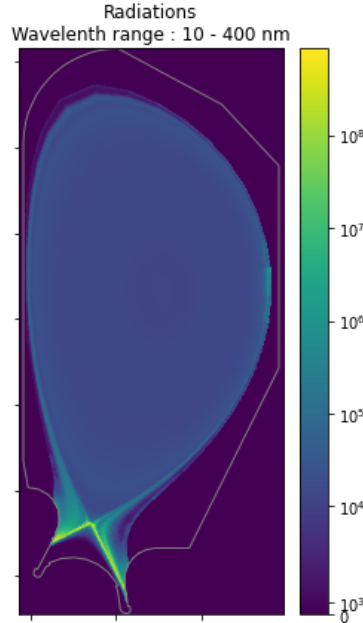

Figure 56: X-ray emitter (in W·m^{-3}, log scale)
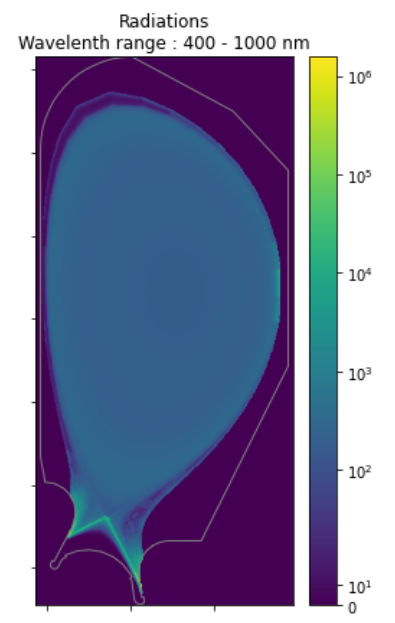
Figure 57: UV emitter (in W·m^{-3}, log scale)

Figure 58: Visible and near IR emitter (in W·m^{-3}, log scale)

13.3 Reconstructions

Reconstructions (figures 59 to 61) are performed with Odstrčil's regularisation and with an adaptive reconstruction parameter (see equation 22) and not the best alpha method. Indeed this emitter is supposed to be realistic, and in order to provide realistic reconstructions a method also used in experimental conditions must be used. Moreover, this adaptive alpha method seems to be already used in experimental conditions [19, 24].
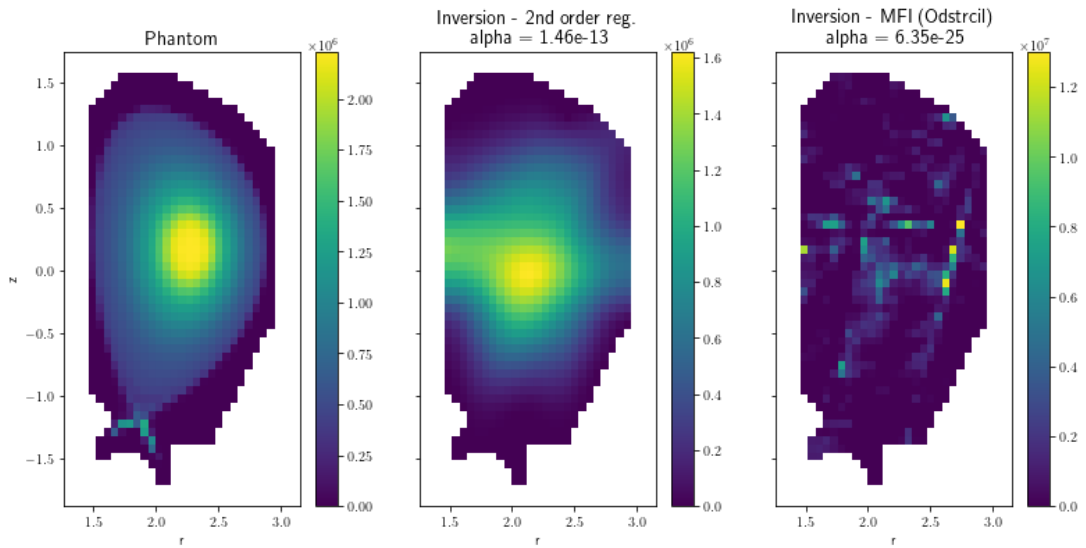
Figure 59: Comparison of the reconstructions for the X-ray emitter with a reconstruction parameter obtained analytically
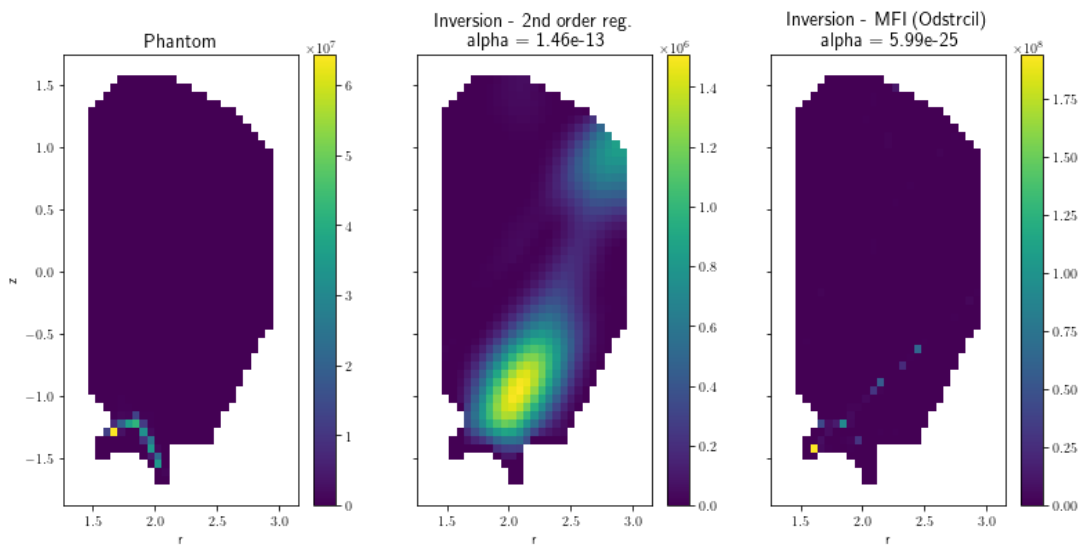

Figure 60: Comparison of the reconstructions for the UV emitter with a reconstruction parameter obtained analytically
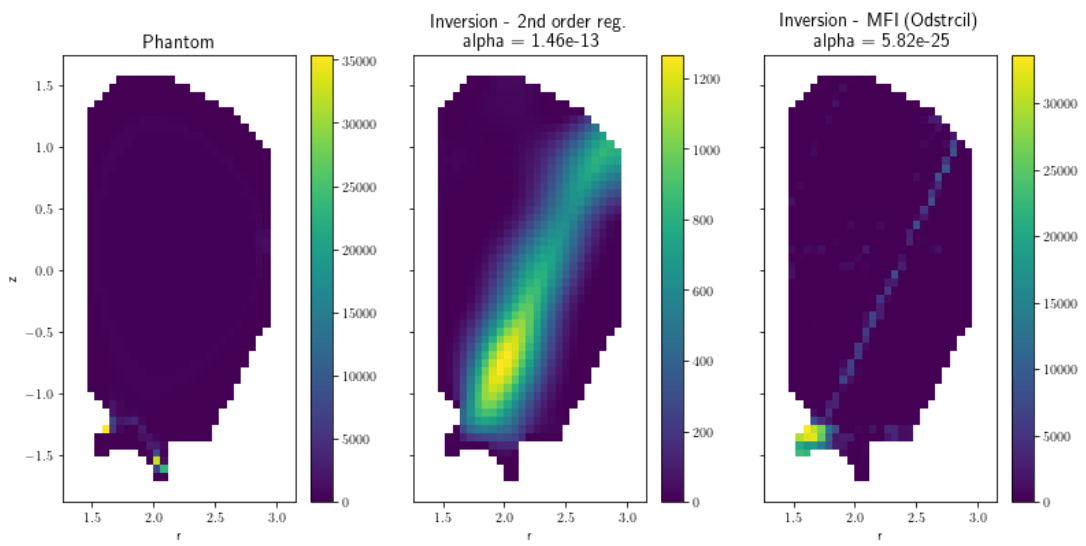

Figure 61: Comparison of the reconstructions for the visible and near IR emitter with a reconstruction parameter obtained analytically

Considering Odstrčil's reconstruction, for the UV and visible-IR domains, emitters are similar to the SOLPS emitter with some perturbation. So it's normal to find similar reconstructions than in section 12.2, meaning a big emission reconstruction with a line artifact. Moreover, reconstructions are pretty good even if the shape of the light emitted is not the same. Furthermore orders of magnitude are similar. In both cases, there is an artifact along a LoS, however this can be easily identified as an artifact since this shape doesn't follow the magnetic surfaces. The shape of the reconstructed emitter in the divertor region is really different from what is expected. However, the section 12.2 shows that these shapes are the best which can be expected when there is a strong emission in the divertor region and perturbations in the core region.

However, it must be kept in mind for the visible domain that some light might be emitted around the limiter surface and that could modify the results of the reconstruction. Simulations with a larger SOLPS mesh is necessary in order to verify this assumption.

Concerning the X-ray domain, the reconstruction with Odstrčil's regularisation is bad. Neither the thin emitter in the divertor region nor the emission in the core region are correctly reconstructed since the result looks more like artifacts. The only good point is that artifacts are located in the region where the light is emitted. However a reconstruction carried with the 2nd order regularisation and the adaptive alpha permit to reconstruct at least the core emitter, the divertor emitter is not reconstructed at all. For the other wavelength range, the 2nd order regularisation outputs just a big artifact, not really representative of the divertor emission.

This analysis shows that Odstrčil regularisation and 2nd order regularisation can be used complementary when a reconstruction method fails to provide a good output.

14 Conclusion

The goal of this internship was to provide a setup for the bolometers in DTT. This setup should include 96 LoS and provide good results for tomography.

In order to solve this issue, the CHERAB code was used to model DTT and bolometers, then to create synthetic observations which permit to perform tomography. Then, a set of emitters was created, analysis were performed and a statistic was designed in order to rank the setups of bolometers.

A setup was issued providing good results for tomography in DTT. This work also permitted to determine which algorithms should perform the inversion : Odstrčil regularisation and 2nd order regularisation to back it up and to verify results. With this method, it was assess that the analytic method can permit to determine the reconstruction parameter in experimental conditions.

However, this work needs to be completed since approximations were made in the geometry (no ports but tiny hole to permit the LoS to see the plasma) which have a direct influence on the solid angle of the LoS, and so, on the observations. Moreover, a finer mesh should be used in order to obtain better results. Introducing the charge exchange model should be interesting too, especially in this case of a detached divertor. And finally, it should be interesting to use other plasma modelled from simulations results in order to have more realistic plasma to test the setups.

Acknowledgements

References

[1] Boudewijn van Milligen. Fusion wiki, 2009. Online, accessed 06-april-2023.

[2] M. Carr, A. Meakins, M. Bernert, P. David, C. Giroud, J. Harrison, S. Henderson, B. Lipschultz, and F. Reimold. Description of complex viewing geometries of fusion tomography diagnostics by ray-tracing. *Review of Scientific Instruments*, 89(8):083506, 2018.

[3] I. Casiraghi, P. Mantica, F. Koelch, R. Ambrosino, B. Baiocchi, A. Castaldo, J. Citrin, M. Dicorato, L. Frasinetti, A. Mariani, P. Vincenzi, P. Agostinetti, L. Aucone, L. Balbinot, S. Ceccuzzi, L. Figini, G. Granucci, P. Innocente, T. Johnson, H. Nyström, and M. Valisa. First principle-based multi-channel integrated modelling in support of the design of the Divertor Tokamak Test facility. *Nuclear Fusion*, 61:116068, 2021.

[4] EUROfusion. *European Research Roadmap to the Realisation of Fusion Energy*. EUROfusion, 2018.

[5] R. Ambrosino. DTT - Divertor Tokamak Test facility: A testbed for DEMO. *Fusion Engineering and Design*, 167:112330, 2021.

[6] Xavier Bonnin, Wouter Dekeyser, Richard Pitts, David Coster, Serguey Voskoboynikov, and Sven Wiesen. Presentation of the new SOLPS-ITER code package for tokamak plasma edge modelling. *Plasma and Fusion Research*, 11:1403102, 2016.

[7] O. Sauter and S. Yu. Medvedev. Tokamak coordinate conventions: COCOS. *Computer Physics Communications*, 184:293, 2013.

[8] H. P. Summer. Atomic Data and Analysis Structure (ADAS) User Manual. `https://www.adas.ac.uk/manual.php`.

[9] H. P. Summer. OPEN-ADAS. `https://open.adas.ac.uk/`.

[10] M. N. A. Beurskens, L. Giudicotti, M. Kempenaars, R. Scanell, and M. J. Walsh. ITER LIDAR performance analysis. *Review of Scientific Instruments*, 79:10E727, 2008.

[11] C. Giroud, A. Meakins, M. Carr, A. Baciero, and C. Bertrand. CHERAB Spectroscopy Modelling Framework. `http://doi.org/10.5281/zenodo.5778961`.

[12] Richard Gordon, Robert Bender, and Gabor T. Herman. Algebraic Reconstruction Techniques (ART) for three-dimensional electron microscopy and X-ray photography. *Journal of Theoretical Biology*, 29(3):471–481, 1970.

[13] A.H. Andersen and A.C. Kak. Simultaneous Algebraic Reconstruction Technique (SART): A superior implementation of the ART algorithm. *Ultrasonic Imaging*, 6(1):81–94, 1984.

[14] M. Anton, H. Weisen, M.J. Dutch, W. Von der Linden, F. Buhlmann, R. Chavan, B. Marletaz, P. Marmillod, and P. Paris. X-ray tomography on the TCV tokamak. *Plasma physics and controlled fusion*, 38(11):1849–1878, 1996.

[15] D. Mazon, D. Vezinet, D. Pacella, D. Moreau, L. Gabelieri, A. Romano, P. Malard, J. Mlynar, R. Masset, and P. Lotte. Soft X-ray tomography for real-time applications: present status at Tore Supra and possible future developments. *Review of Scientific Instruments*, 83(6):063505, 2012.

[16] J. Mlynar, M. Imrisek, V. Weinzettl, M. Odstrcil, J. Havlicek, F. Janky, B. Alper, and A. Murari. Introducing minimum Fisher regularisation tomography to AXUV and soft X-ray diagnostic systems of the COMPASS tokamak. *Review of Scientific Instruments*, 83(10):10E531, 2012.

[17] M. Odstrcil, J. Mlynar, T. Odstrcil, B. Alper, and A. Murari. Modern numerical methods for plasma tomography optimisation. *Nuclear Instruments and Methods in Physics Research Section A: Accelerators, Spectrometers, Detectors and Associated Equipment*, 686:156–161, 2012.

[18] Alessandro Cultrera and Luca Callegaro. A simple algorithm to find the L-curve corner in the regularisation of ill-posed inverse problems. *IOP SciNotes*, 1(2):025004, 2020.

[19] Pierre David. *Tomography in a linear magnetised plasma*. PhD thesis, Aix-Marseille Université, 2017.

[20] M. Carr, A. Meakins, A. Baciero, M. Bernert, A. Callarelli, A. Field, C. Giroud, J. Harrison, N. Hawkes, S. Henderson, B. Lipshultz, T. Lunt, D. Moulton, and F. Reimold. Towards integrated data analysis of divertor diagnostics with ray-tracing. In *44th EPS Conference on Plasma Physics*. European Physical Society, 2017.

[21] M. Carr, A. Meakins, S.A. Silburn, J. Karhunen, M. Bernert, C. Bowman, A. Callarelli, P. Carvalho, C. Giroud, J.R. Harrison, S. Henderson, A. Huber, B. Lipshultz, T. Lunt, D. Moulton, and F. Reimold. Physically principled reflection models applied to filtered camera imaging inversions in metal walled fusion machines. *Review of Scientific Instruments*, 90(4):043504, 2019.

[22] A. Meakins and M Carr. Raysect Python Raytracing Package. `http://doi.org/10.5281/zenodo.1205063`.

[23] Claudio Mancinelli, Marco Livesu, and Enrico Puppo. Gradient field estimation on triangle meshes. In *Eurographics Proceedings*. The Eurographics Association, 2018.

[24] A. Jardin, I. Bielecki, D. Mazon, Y. Peysson, K. Król, D. Dworak, and M. Sholz. Implementing an X-ray tomography method for fusion devices. *The European Physical Journal Plus*, 136:706, 2021.